INCORPORATION OF LONGITUDINAL STRESS COUPLING INTO A MAP-PLANE FINITE ELEMENT GLACIER FLOW MODEL

by

BRUCE HAMILTON RAUP

B. S., Washington University in St. Louis, 1987

A thesis submitted to the

Faculty of the Graduate School of the

University of Colorado in partial fulfillment

of the requirements for the degree of

Master of Science

Department of Geological Sciences

1995

This thesis for the Master of Science degree by

Bruce Hamilton Raup

has been approved for the

Department of

Geological Sciences

by

Mark F. Meier

W. Tad Pfeffer

Date _____

Raup, Bruce Hamilton (M. S., Geological Sciences)

Incorporation of Longitudinal Stress Coupling into a Map-Plane Finite Element Glacier Flow Model

Thesis directed by Professor Mark F. Meier

A map-plane finite element model designed for modeling the flow of ice sheets was modified to include inter-element coupling of longitudinal stresses. Although this coupling acts only along flow lines, it results in more realistic simulation of the flow of glacier ice. An example is presented which compares the model results before and after the implementation of this stress coupling. This new model is then applied to an ice dome on the Labrador Peninsula, in an attempt to reconstruct a late glacial advance of ice across Hudson Strait, Arctic Canada, which has been indicated by geomorphological evidence.

CONTENTS

FIGURES

FIGURE

TABLES

TABLE

CHAPTER 1

INTRODUCTION

Reconstruction of events related to the waning of the Laurentide Ice Sheet from its Late Quaternary maximum extent is important in understanding the ice sheet's effects on climate, and how it was affected by climate. Temperature records from ice cores show several periods of sudden cooling which occurred as the planet was emerging from the Last Glacial Maximum at ca. 20,000 years before present (20 ka BP), one of which is an event known as the Younger Dryas (ca. 11–10 ka BP) [25, 13]. Marine sediments dating from the same time indicate episodes of high iceberg flux from the vicinity of the northwest Atlantic into the north-central and central Atlantic (see, for example, [2]). It is thought that by disrupting the formation of North Atlantic Bottom Water, icebergs and meltwater from the Laurentide Ice Sheet caused a chain of events which may have temporarily reversed the warming trend associated with deglaciation [18]. This type of ice sheet – climate interaction, as well as the specific processes by which the above event may have occurred, can be better understood through ice sheet modeling. This thesis describes the implementation of longitudinal stress coupling in an existing finite element model, with the objective of improving its ability to simulate ice-sheet dynamics. A specific event is simulated which occurred around the time of the last deglaciation. The following two sections describe the original model and the need to improve it.

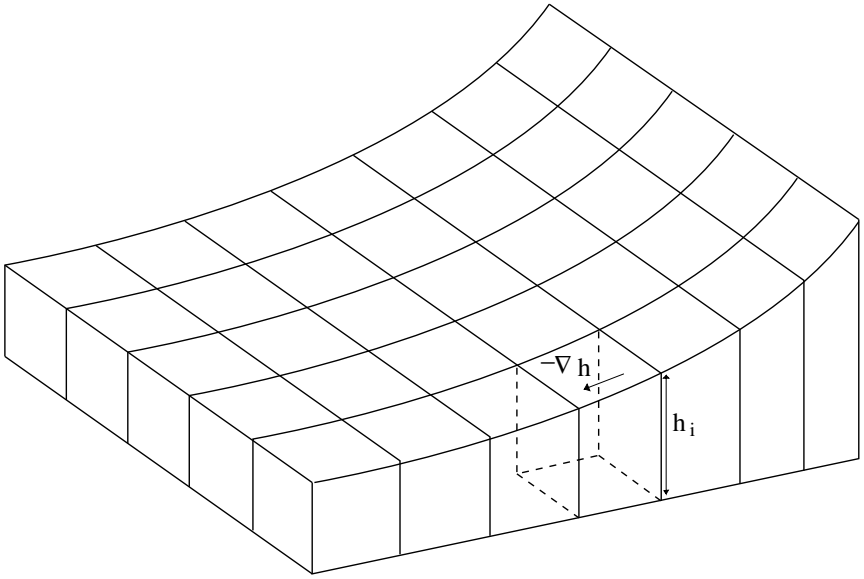

Figure 1.1: Finite element mesh of the Fastook model.

1.1 Description of Original Model

James Fastook developed a two-dimensional ("map plane") finite element model to aid in the reconstruction of ice sheets [15]. Rather than solve force balance equations, the model assigns a vertically averaged velocity to each element as determined according to the surface gradient; the continuity equation is then used to determine how the ice thickness changes in response to converging and diverging flow. Accumulation and ablation are also taken into account.

1.1.1 Program Features The Fastook program's features are summarized as follows:

- Map-plane finite-element model: two-dimensional element grid is used to calculate ice elevations at nodes, giving an implicit third dimension to the model. (See Figure 1.1.)
- Velocity and flux are determined for each element based on the forces arising from the gradient of surface elevation, and on non-linear constitutive properties for ice flow (Glen's flow law).
- Mass balance may be specified, and is taken into account at each node.
- At each time step, the mass continuity equation is solved to determine the new ice surface elevations at the nodes.

At each time step, the model calculates the surface slope of the ice in each element. This slope is then used to calculate flow and sliding velocities of the ice, and hence ice flux. Taking into account accumulation and ablation, as well as converging and diverging flow, the continuity equation is used to solve for the resulting change in ice elevations at the nodal points at each time step.

1.1.2 Internal Deformation Glen's Flow Law is used to calculate the speed of the ice due to internal deformation [29]:

$$U_f = \frac{2}{n+2}\left(\frac{\tau_b}{A}\right)^3 H \tag{1.1}$$

where U_f is the flow velocity (due to internal deformation), τ_b is the basal driving shear stress, and A is the flow law parameter. A value of $3\,\text{bar year}^{1/3}$ was generally used for A [29].

1.1.3 Sliding A Weertman power-law sliding relation is used [34]:

$$U_s = \left(\frac{\tau_b}{B}\right)^2 \tag{1.2}$$

where U_s is the sliding velocity, τ_b is again the basal driving shear stress, and B is a sliding parameter. A value of $0.02\,\text{bar year}^{1/2}\ m^{-1/2}$ is generally used for B, based on a calibration experiment in which Fastook compared model output with measured ice geometry and velocities in Antarctica and Greenland [15].

1.1.4 Calving Calving is not simulated in the original model.

1.2 Motivation for Changes to Model

Geomorphological evidence indicates that at some time in the past, ice crossed from the Labrador Peninsula over Hudson Strait to southern Baffin Island. In order to under stand the ice dynamics of this event, Tad Pfeffer applied James Fastook's model, augmented by a simple iceberg calving law, to an ice dome on Labrador approximately 2000 m thick (unpublished). By adjusting boundary conditions such as basal sliding parameters and calving criteria, he searched for conditions that would lead to ice crossing Hudson Strait. This model, which included no inter-element coupling of forces, produced no ice flow across the strait. There are two possible causes for this result: either the model

was correct and it is not glaciologically feasible for ice from a Labrador ice dome of that thickness to cross Hudson Strait, or the ice dynamics incorporated into the model were insufficient to capture this type of ice flow realistically.

The application of the present model to this same problem, discussed at greater length in Chapter 5, shows that simplifications in the previous model led to the model result of ice not crossing Hudson Strait. The addition of longitudinal stress coupling in the present model enabled it to model ice flow across the strait; it indeed seems feasible for ice actually to have crossed Hudson Strait in the past.

The next chapter describes the theory underpinning the original Fastook model, as well as the theory behind the changes made to implement inter-element stress coupling. Chapter 3 discusses the practical aspects of the actual implementation. Chapter 4 compares the results of the old and new models when applies to a simple test problem. Finally, Chapter 6 summarizes the work and discusses the results and possible improvements.

CHAPTER 2

THEORY

This chapter begins with a discussion of the theory behind the original model (henceforth called the Fastook model), and then describes the modifications made to this model.

2.1 Summary of Symbols

- $\dot{a}$ net mass balance (units: length (ice-equivalent)/time)
- A flow parameter in Glen's Flow Law
- B sliding law parameter
- f fraction of sliding versus creep velocity
- g gravitational acceleration
- G stress-gradient modification to driving stress
- h surface elevation of ice
- H ice thickness measured vertically
- k linearization constant relating flux to surface slope
- λ parameter in linearization of G term
- m sliding law exponent
- n flow law exponent
- ρ density of ice

$\vec{\sigma}$	flux of ice (units: length^2/time)
t	time coordinate
τ_0	cross-over stress for linear / non-linear term in G
τ_b	driving stress
τ_{xx}	normal stress in the along-flow direction
τ_{zx}	shear stress
$u(z)$	flow velocity in the x-direction
$\vec{U}$	total depth-averaged velocity
$\vec{U}_f$	depth-averaged flow velocity
$\vec{U}_s$	sliding velocity
x	coordinate in direction of flow, in plane of surface
y	horizontal coordinate across flow
z	vertical coordinate
overbar	depth-averaging operator: $\overline{X} = \frac{1}{H}\int_0^H X dz$

A vector quantity without the vector symbol ($\vec{}$) is taken to be the magnitude. For example, $U_f \equiv |\vec{U}_f|$.

The Fastook model is based on solving the continuity equation. The ice sheet or glacier is broken into elements. The velocity (vertically averaged) of each element is determined solely from the surface slope of that element, and is independent of all other elements. The continuity equation is solved, and the height of the ice (the ice thickness) at each node is adjusted to account for converging and diverging flow. This model handles divergence of flow of any nature, whether due to flow lines changing their distance from one another, or a change of speed along flow lines.

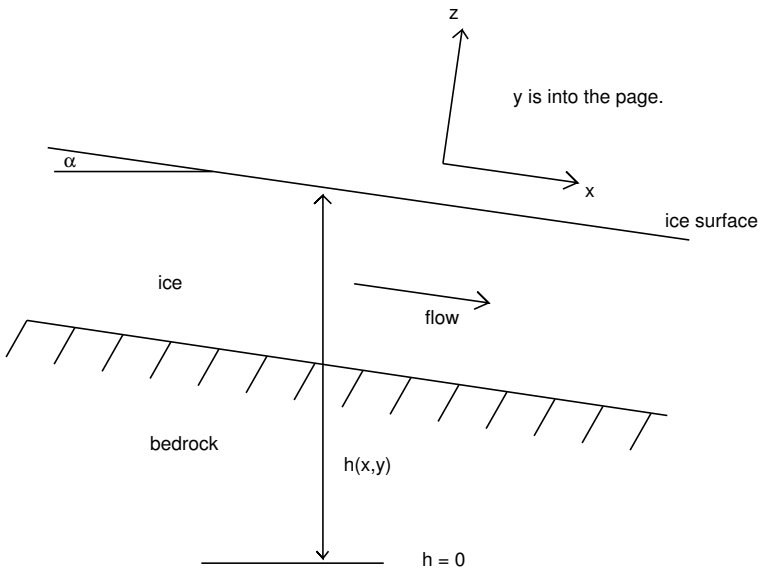

Figure 2.1: Coordinate system.

The coordinate system is shown in Figure 2.1. Small angle approximations are used; for example, distances measured vertically are measured along the z-axis.

The continuity equation (with dimensions Length / Time) is

$$\frac{\partial h}{\partial t} = \dot{a}(x,y) - \nabla \cdot \vec{\sigma}(x,y) \tag{2.1}$$

where

$\vec{\sigma}(x,y)$ is the flux of ice per unit width

$\dot{a}(x,y)$ is the net accumulation or ablation rate at the surface due to precipitation, melting, and sublimation. This is the same as $\dot{b}$ in [29].

$h = h(x,y)$ is the surface elevation of the ice, measured vertically from an appropriate datum.

The flux $\vec{\sigma}$ can also be expressed as

$$\vec{\sigma} = \vec{U} H \tag{2.2}$$

where

$\vec{\sigma}(x,y)$ is the flux of ice

$\vec{U}$ is the vertically averaged ice velocity

H is the ice thickness measured vertically

Note that h and H are related via the bed topography.

The flux can be expressed

$$\vec{\sigma}(x,y) = -k(x,y)\nabla h \tag{2.3}$$

In this expression, the surface gradient ∇h, which lies in the x-y plane and points in the direction of maximum uphill slope, determines the direction of $\vec{\sigma}$. An expression for $k(x,y)$ will be developed below.

2.2 Expressions for Velocity

The following derivation of the flow velocity assumes plane strain, and follows the development of Fastook in [15]. Assuming, for the moment, that deformational creep is the only component of velocity (basal sliding will be considered later), the non-linear constitutive law for ice relates the vertical gradient of the x-component of the velocity to the shear stress as

$$\frac{1}{2}\frac{\partial u}{\partial z} = \left(\frac{\tau_{zx}(z)}{A}\right)^n \tag{2.4}$$

When the surface slope ∇h is in the x-direction, $\tau_{zx}(z) = \rho g|\nabla h|(H - z)$, and thus

$$\frac{1}{2}\frac{\partial u}{\partial z} = \left[\frac{\rho g|\nabla h|(H - z)}{A}\right]^n \tag{2.5}$$

where

- u is the (scalar) velocity in x-direction $= u(z)$
- z is the vertical coordinate, with $z = 0$ at the bed and $z = H$ at the surface
- H is the ice thickness (as before)
- A is a constant
- ρ is the density of ice
- g is the gravitational acceleration
- n is an empirical exponent, usually taken to be 3.

Integrating with respect to z from the bed to an arbitrary depth, we have

$$\begin{aligned} u(z) &= \frac{2}{A^n}(\rho g|\nabla h|)^n \int_0^z (H - z')^n dz' \\ &= \frac{2}{n+1}\left[\frac{\rho g|\nabla h|}{A}\right]^n \left[H^{n+1} - (H - z)^{n+1}\right] \end{aligned} \tag{2.6}$$

We want the vertically averaged velocity. Assuming that the direction of ∇h coincides with the x-axis, the magnitude of the vertically averaged velocity (in the x-direction) is given by

$$\begin{aligned} U_f &= \frac{1}{H}\int_0^H u(z)dz \\ &= \frac{1}{H}\frac{2}{n+1}\left[\frac{\rho g|\nabla h|}{A}\right]^n \int_0^H (H^{n+1} - (H-z)^{n+1})dz \\ &= \frac{2}{n+2}\left[\frac{\rho g|\nabla h|}{A}\right]^n H^{n+1} \end{aligned} \tag{2.7}$$

More generally, the depth-averaged flow velocity $\vec{U}_f$ can be expressed as a vector quantity, as

$$\vec{U}_f = \frac{2}{n+2}\left[\frac{\rho g|\nabla h|}{A}\right]^n H^{n+1}\left(\frac{-\nabla h}{|\nabla h|}\right) \tag{2.8}$$

The sliding of a glacier on its bed is complicated and not well understood; for the sliding velocity, the following empirical form developed by Weertman [34] is generally used:

$$\vec{U}_s = \left[\frac{\rho g|\nabla h|}{B}\right]^m H^m\left(\frac{-\nabla h}{|\nabla h|}\right) \tag{2.9}$$

In the expressions for $\vec{U}_f$ and $\vec{U}_s$, A and B are constants which depend on a variety of physical properties of the ice, bed, and ice-bed interface. The direction of the velocity, in both cases, is determined to be in direction of the maximum downhill slope (that is, in the direction of $-\nabla h$).

In the original Fastook model, $\vec{U}_f$ and $\vec{U}_s$ are combined in an adjustable weighted sum:

$$\vec{U} = f\vec{U}_s + (1-f)\vec{U}_f,$$

where f acts as a sort of "knob" which controls the relative importance of U_s and U_f. It would be an improvement to eliminate this f, so that

$$\vec{U} = \vec{U}_f + \vec{U}_s$$

The relative magnitudes can be adjusted through A and B, which have a more physical basis than does f. For consistency with the Fastook model, however, f will be retained in the present modification.

Now we can write down what $k(x,y)$ is:

$$\begin{aligned} k &= \frac{|\sigma|}{|\nabla h|} = |\nabla h|^{-1} UH \\ &= H|\nabla h|^{-1}\left[f\left(\frac{\rho g|\nabla h|}{B}\right)^m H^m + (1-f)\frac{2}{n+2}\left(\frac{\rho g|\nabla h|}{A}\right)^n H^{n+1}\right] \\ &= f\left(\frac{\rho g}{B}\right)^m |\nabla h|^{m-1} H^{m+1} + (1-f)\frac{2}{n+2}\left(\frac{\rho g}{A}\right)^n |\nabla h|^{n-1} H^{n+2} \end{aligned} \quad (2.10)$$

In the above, it was implicitly assumed that $|\vec{U}| = |\vec{U}_f| + |\vec{U}_s|$. This is indeed the case, since $\vec{U}_f$ and $\vec{U}_s$ always point in the same direction. Substituting $k\nabla h$ for $\vec{\sigma}$, the differential equation can be expressed as

$$\frac{\partial h}{\partial t} = \dot{a} - \nabla \cdot (-k\nabla h) \quad (2.11)$$

2.3 Alternative forms for $\vec{U}_f$ and $\vec{U}_s$

From Equation 2.7, the magnitude of the vertically averaged velocity U_f (due only to internal deformation) is

$$\begin{aligned} U_f &= \frac{2}{n+2}\left[\frac{\rho g|\nabla h|}{A}\right]^n H^{n+1} \\ &= \frac{2}{n+2}\left[\frac{\rho g H|\nabla h|}{A}\right]^n H \\ &= \frac{2}{n+2}\left[\frac{\tau_b}{A}\right]^n H \end{aligned} \quad (2.12)$$

where τ_b is the basal shear stress ($\tau_b = \tau_{xy}|_{bed}$).

The expression for τ_b above includes only the stress due to the local surface slope (i.e., the average slope over the element under consideration). In reality, surrounding ice can exert pushing and pulling forces if velocity gradients are present.

As a first step toward accounting for the influences of the surrounding ice, the expression for the basal driving stress τ_b was modified to include stresses arising from gradients in the longitudinal (along-flow) stress τ_{xx}. The theory behind this modification is established in the glaciological literature (e.g. [8]), and is derived in the appendix entitled "Derivation of the 'G' term."

With the first longitudinal stress gradient term, the basal shear stress has the form

$$\tau_b = \rho g H |\nabla h| + 2G \tag{2.13}$$

where

$$G = H \frac{\partial \overline{\tau}_{xx}}{\partial x} \tag{2.14}$$

Here, the overline indicates averaging over the ice thickness. τ_{xx} is the deviatoric stress which is equal to $\sigma_{xx} - P$ (where P is the hydrostatic pressure).

For use in the model, the vertically averaged longitudinal stress τ_{xx} must be expressed in terms of velocity, which is a variable of the model. This is done as follows. Glen's flow law, for the longitudinal component, is

$$\tau_{xx} = A \left(\frac{\partial u(z)}{\partial x} \right)^{\frac{1}{n}} \tag{2.15}$$

where $u(z)$ is the **total** velocity (flow plus sliding) in the x-direction, which can depend on depth z. Averaging with depth, Equation 2.15 becomes

$$\overline{\tau}_{xx} = \frac{1}{H} A \int_0^H \left(\frac{\partial u(z)}{\partial x} \right)^{\frac{1}{n}} dz \tag{2.16}$$

Here it is assumed that $\partial u(z)/\partial x$ is independent of z. This is a result of the plane-strain assumption, as well as the assumption of constant slope and thickness, as discussed in [29]. In reality, it is known that $\partial u(z)/\partial x$ does indeed depend on z [29]. With this assumption, the averaging does not change the

integrand, and we have

$$\overline{\tau}_{xx} = A\left(\frac{\partial u(z)}{\partial x}\right)^{\frac{1}{n}} \tag{2.17}$$

Also, since $\partial u(z)/\partial x$ is assumed to be independent of z,

$$\frac{1}{H}\int_0^H \frac{\partial u(z)}{\partial x}dz = \frac{\partial u(z)}{\partial x} \tag{2.18}$$

Additionally, assuming H varies negligibly with x,

$$\frac{1}{H}\int_0^H \frac{\partial u(z)}{\partial x}dz = \frac{\partial}{\partial x}\overline{u(z)} = \frac{\partial U}{\partial x} \tag{2.19}$$

Combining these yields

$$\frac{\partial u(z)}{\partial x} = \frac{\partial U}{\partial x} \tag{2.20}$$

which, when combined with the expression for $\overline{\tau}_{xx}$ in Equation 2.17, yields

$$\overline{\tau}_{xx} = A\left(\frac{\partial U}{\partial x}\right)^{\frac{1}{n}} \tag{2.21}$$

Again, U is the total vertically averaged velocity. The new τ_b can now be written

$$\begin{aligned} \tau_b &= \rho g H|\nabla h| + 2G \\ &= \rho g H|\nabla h| + 2AH\frac{\partial}{\partial x}\left(\frac{\partial U}{\partial x}\right)^{\frac{1}{n}} \end{aligned} \tag{2.22}$$

Equation 2.12 on page 12 expresses U_f in terms of τ_b. To arrive at the new modified expression for flow velocity, the new expression for τ_b replaces the τ_b in Equation 2.12. Expressed in vector form, $\vec{U}_f$ is

$$\vec{U}_f = \frac{2}{n+2}\left(\frac{\tau_b}{A}\right)^n H\left(\frac{-\nabla h}{|\nabla h|}\right) \tag{2.23}$$

$$= \frac{2H}{(n+2)A^n}\left[\rho g H|\nabla h| + 2AH\frac{\partial}{\partial x}\left(\frac{\partial U}{\partial x}\right)^{\frac{1}{n}}\right]^n \left(\frac{-\nabla h}{|\nabla h|}\right) \tag{2.24}$$

To arrive at a similar expression for $\vec{U}_s$, the new τ_b is substituted into the previous expression $U_s = (\tau_b/B)^m$

$$\vec{U}_s = B^{-m}\left[\rho g H|\nabla h| + 2AH\frac{\partial}{\partial x}\left(\frac{\partial U}{\partial x}\right)^{\frac{1}{n}}\right]^m \left(\frac{-\nabla h}{|\nabla h|}\right) \tag{2.25}$$

Recall that U is the total velocity magnitude $fU_s + (1-f)U_f$.

More properly, to arrive at the new expressions for $\vec{U}_f$ and $\vec{U}_s$, a modified expression for $\tau_{zx}(z)$ should be inserted into Equation 2.4, which should then be integrated twice as before. However, the derivation of the G-term leaves us with only a new expression for τ_b, the shear stress at the bed. It is recognized that the simple modification of Equation 2.12 is only an approximation.

The new expression for $k(x,y)$ can be written as

$$\begin{aligned} k(x,y) &= \frac{H}{|\nabla h|}\left[fU_s + (1-f)U_f\right] \\ &= \frac{H}{|\nabla h|}\left[fB^{-m}\tau_b^m + (1-f)\frac{2H}{A^n(n+2)}\tau_b^n\right] \end{aligned} \tag{2.26}$$

where, again, τ_b is given by

$$\tau_b = \rho g H|\nabla h| + 2AH\frac{\partial}{\partial x}\left(\frac{\partial U}{\partial x}\right)^{\frac{1}{n}} \tag{2.27}$$

Note that since $\vec{U}_f$ and $\vec{U}_s$ are in the same direction $(-\nabla h/|\nabla h|)$, the magnitude of the sum of the two is equal to the sum of their magnitudes.

Because a derivative is being taken of a quantity raised to the $1/n$ power (where $n = 3$), the derivative becomes problematically large when that quantity approaches zero. This problem can be resolved by linearizing the term as it approaches zero. Carrying out the derivative, we have

$$\frac{\partial}{\partial x}\left(\frac{\partial U}{\partial x}\right)^{\frac{1}{n}} = \frac{1}{n}\frac{\partial^2 U}{\partial x^2}\left(\frac{\partial U}{\partial x}\right)^{\frac{1-n}{n}} \tag{2.28}$$

To keep this term from becoming excessively large as $\partial U/\partial x$ approaches zero, the following substitution is made:

$$\frac{1}{\left(\frac{\partial U}{\partial x}\right)^{\frac{n-1}{n}}} \Rightarrow \frac{1}{\left(\frac{\partial U}{\partial x}\right)^{\frac{n-1}{n}} + \lambda} \tag{2.29}$$

so that

$$\tau_b = \rho g H |\nabla h| + \frac{2}{n} A H \frac{\partial^2 U}{\partial x^2} \frac{1}{\left(\frac{\partial U}{\partial x}\right)^{\frac{n-1}{n}} + \lambda} \tag{2.30}$$

The effect of λ is illustrated in Figure 2.2.

Now what is λ? Contributions of the two terms in the denominator of the G-term are equal when $\left(\frac{\partial U}{\partial x}\right)^{\frac{n-1}{n}} = \lambda$. It is useful to express λ in terms of a corresponding stress τ_0. Using Glen's Flow Law,

$$\frac{\partial U}{\partial x} = \left(\frac{\tau_{xx}}{A}\right)^n \tag{2.31}$$

we have

$$\left(\frac{\partial U}{\partial x}\right)^{\frac{n-1}{n}} = \lambda = \left(\frac{\tau_0}{A}\right)^{n\frac{n-1}{n}} = \left(\frac{\tau_0}{A}\right)^{n-1} \tag{2.32}$$

The parameter τ_0 is to be specified by the user of the model.

2.4 Summary of Assumptions

(1) Deformation is plane strain locally. Validity of this depends on the flow configuration.

(2) $\frac{\partial u(z)}{\partial x}$ is independent of z.

(3) Strain is purely shear, so that $\dot{\varepsilon}_{ij} = \left(\frac{\tau_{ij}}{A}\right)^n$ (page 10).

(4) Strain is purely axial, so that $\dot{\varepsilon}_{ij} = \left(\frac{\tau_{ij}}{A}\right)^n$, even for i=j=1 (page 13).

(5) Variation of H (the thickness of the ice) with x is negligible (i.e., $\partial H/\partial x \approx 0$).

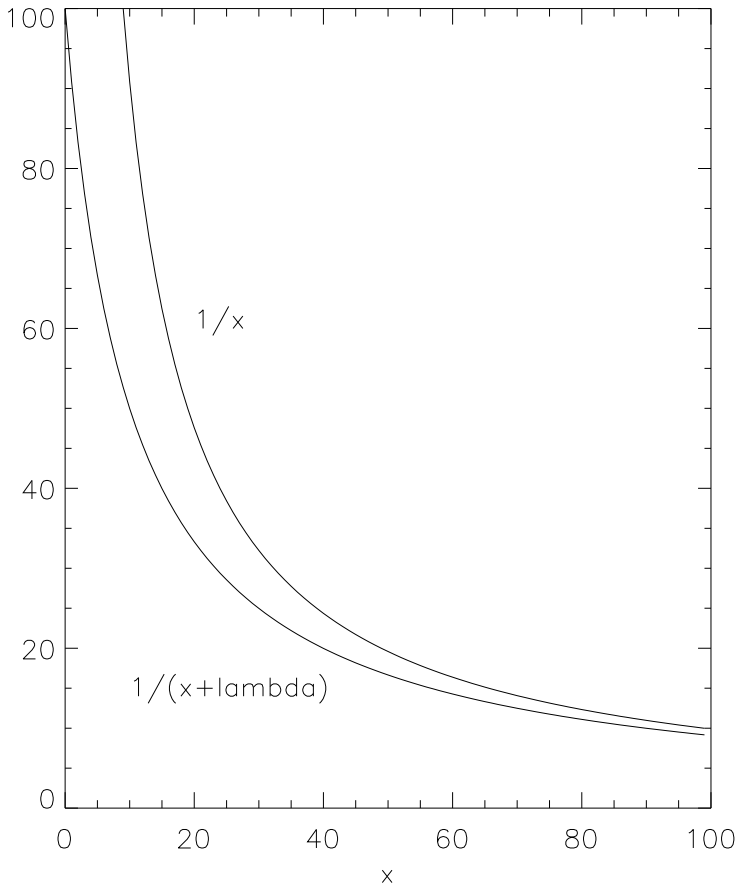

Figure 2.2. Comparison of derivative term before and after linearization. Units are arbitrary.

2.5 Discussion of $\sigma = k(x,y)\nabla h$

It may be noticed that in this new formulation, the expression for the flux, Equation 2.3, remains unchanged. On first look, it appears that the ice flux will be small when the surface slope ∇h is small. In the old formulation (without longitudinal stress coupling), this was indeed true. Since

$$k = \frac{UH}{|\nabla h|} \tag{2.33}$$

and because the old expression for the total velocity U includes ∇h in every term, the old expression for k contains only terms with ∇h raised to positive powers.

In the new expression for total velocity U, however, there are terms which do not contain ∇h, so that the new expression for k contains terms with ∇h in the denominator. This leads to two slightly different manifestations of the same effect:

(1) k can be very large when ∇h is small, and

(2) k becomes infinite when ∇h is zero.

The first effect above is desirable, as it allows the rapid movement of elements which are being pushed from above or pulled from below, yet which have small surface slope themselves. The second effect above is a problem, which was resolved by never allowing a non-zero ∇h to be less than 10^{-9}. More precisely, the program goes through the following steps: the true surface slope ∇h is calculated for the current element. If this is equal to zero, then the stress-coupling term becomes equal to zero. (This is because when the element has zero slope, the direction of flow becomes difficult to define; the unit vector defining that direction is therefore set to zero.) If the slope is non-zero, the direction of flow is taken to be the direction of maximum downward slope. If

the magnitude of the slope $|\nabla h|$ is less than 10^{-9}, it is set to 10^{-9}.

It is useful to compare the old and new expressions for σ in the following way. The old expression for σ is

$$\begin{aligned}\sigma_{old} &= HU_{old} \\ &= Hf\left(\frac{\tau_b}{B}\right)^m + H(1-f)\frac{2H}{n+2}\left(\frac{\tau_b}{A}\right)^n \end{aligned} \tag{2.34}$$

Similarly, the expression for σ_{new} is obtained by replacing τ_b by τ_{new}:

$$\begin{aligned}\sigma_{new} &= HU_{new} \\ &= Hf\left(\frac{\tau_{new}}{B}\right)^m + H(1-f)\frac{2H}{n+2}\left(\frac{\tau_{new}}{A}\right)^n \end{aligned} \tag{2.35}$$

where

$$\tau_{new} = \tau_b + G_0 \tag{2.36}$$

Here, $\tau_b = \rho g H|\nabla h|$, and G_0 is the new stress-coupling term, and is given by

$$G_0 = \frac{2}{n}AH\frac{\partial^2 U}{\partial x^2}\frac{1}{\left(\frac{\partial U}{\partial x}\right)^{\frac{n-1}{n}} + \lambda} \tag{2.37}$$

Setting $m = 2$ and $n = 3$, and expanding the terms τ_{new}^m and τ_{new}^n to $\tau_b^2 + G_0^2 + 2\tau_b G_0$ and $\tau_b^3 + G_0^3 + 3\tau_b^2 G_0 + 3\tau_b G_0^2$ respectively, we have

$$\begin{aligned}\sigma_{new} &= Hf\left(\frac{\tau_b}{B}\right)^2 \\ &\quad + H(1-f)\frac{2H}{3+2}\left(\frac{\tau_b}{A}\right)^3 \\ &\quad + \frac{Hf}{B^2}(G_0^2 + 2\tau_b G_0) \\ &\quad + H(1-f)\frac{2H}{(3+2)A^3}(G_0^3 + 3\tau_b^2 G_0 + 3\tau_b G_0^2) \\ &= \sigma_{old} + \frac{fH}{B^2}(G_0^2 + 2\tau_b G_0) \\ &\quad + (1-f)\frac{2H^2}{5A^3}(G_0^3 + 3\tau_b^2 G_0 + 3\tau_b G_0^2) \qquad (2.38) \\ &\equiv \sigma_{old} + \sigma_{add} \qquad (2.39)\end{aligned}$$

Here, σ_{add} has been introduced for simplicity.

The routine **nconst.f** calculates k, which is used later in the program in combination with the flux to solve the continuity equation. The new "constant" k is given by

$$\frac{1}{|\nabla h|}(\sigma_{old} + \sigma_{add}) \tag{2.40}$$

When $|\nabla h|$ is small, σ_{old} may be negligible compared to σ_{add} in 2.39, so that

$$\sigma_{new} = k_{new}\nabla h \approx \sigma_{add} \tag{2.41}$$

Of course, there is a potential numerical problem with calculating a large k, then multiplying it by a small ∇h in order to get a finite number. But because all calculations are done in double precision arithmetic, and since $|\nabla h|$ cannot be less than 10^{-9} (which is small in the context of surface slopes on an ice sheet, but not so small in the range of double precision numbers), this does not present a problem in practice.

If the new term σ_{add} were not folded into k, but were left outside, so that

$$\sigma = k\nabla h + \text{newterm}$$

the mathematical form would be the same, but this would complicate the solution of the resulting equations by the finite element method. Instead of the continuity equation having a term like $\nabla \cdot k\nabla h$, which is easily transformable via vector calculus identities into a weak variational form amenable to finite element solution ([15]), we would have a term like $\nabla \cdot (k\nabla h + \ldots)$. Rather than completely reformulate the finite element equations, the expression for k was simply changed.

CHAPTER 3

IMPLEMENTATION OF CHANGES TO MODEL

The previous chapter describes the theory leading up to the new expression for τ_b, the driving stress at the bed. This new expression (Equation 2.30) includes spatial derivatives of the velocity field. This chapter addresses the algorithms related to calculating these derivatives. In particular, Section 3.1 describes how gradients are taken generally in this finite element model, then extends this to directional derivatives. Section 3.2 describes the lookup table **ikx**, a data structure used to find the neighboring elements to a given element. Section 3.3 discusses the spatial averaging of the velocity field, done to 1) prevent numerical errors from becoming amplified, and 2) to ensure the proper coupling length for the stress coupling.

3.1 Calculation of $\partial^2 U/\partial x^2$

In the following discussion, as in the model, the ice height h is defined at the mesh nodes, while the velocity U is defined at the element centers. This is because the velocity of a particular element is calculated from the ice heights defined at the four nodes of that element.

In the original model, the driving stress τ_b was calculated as

$$\tau_b = \rho g H |\nabla h|. \tag{3.1}$$

In the above sections, a new expression for τ_b was derived:

$$\tau_b = \rho g H |\nabla h| + \frac{2}{n} A H \frac{\partial^2 U}{\partial x^2} \frac{1}{\left(\frac{\partial U}{\partial x}\right)^{\frac{n-1}{n}} + \lambda} \tag{3.2}$$

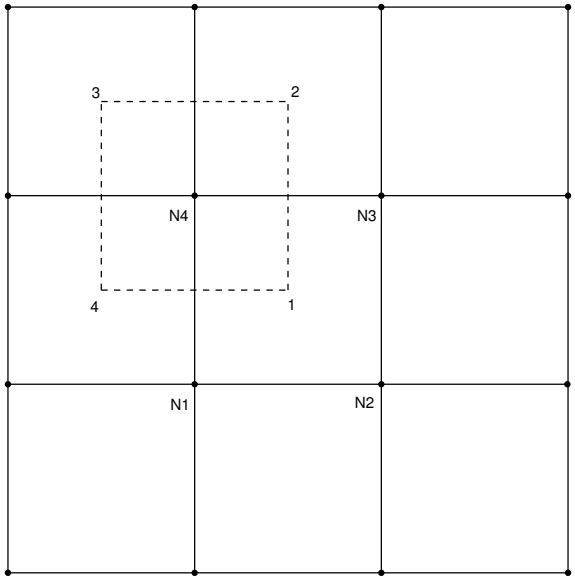

Figure 3.1: Illustration of "Pseudo-element"

In that derivation, U was assumed to be in the x-direction, so the derivatives are in the direction of flow. Plane-strain was assumed.

In the actual model, which is essentially two-dimensional in the map plane, the velocity can have both x- and y-components. Thus $\frac{\partial}{\partial x}$ must be replaced by $\frac{\partial}{\partial l}$, defined to be the derivative in the direction of flow. Such a directional derivative is given by

$$\frac{\partial}{\partial l} = \hat{m} \cdot \nabla \tag{3.3}$$

where $\hat{m}$ is a unit vector in the direction of l. This direction is given by

$$\hat{m} \equiv m_x \hat{\mathbf{i}} + m_y \hat{\mathbf{j}} = \frac{-\nabla h}{|\nabla h|} \tag{3.4}$$

where m_x and m_y are the x- and y-components of $\hat{m}$, respectively. That is, the direction of flow for each element is in the direction of the maximum downward slope of that element. Thus, the desired directional derivative $\frac{\partial}{\partial l}$ is reduced to the dot product between a unit vector in the direction of flow, and a gradient. The following paragraphs describe how the gradient is calculated in a finite element.

The gradient within an element of a quantity defined at the nodes of that element can be easily calculated using the derivatives of the shape functions [3]. For example, in both the old and new versions of the program, the gradient of the ice height (h) is calculated as[1]

$$\nabla h(\xi,\eta) = \hat{\mathbf{i}} \sum_{i=1}^{4} h_i \frac{\partial \phi_i(\xi,\eta)}{\partial x} + \hat{\mathbf{j}} \sum_{i=1}^{4} h_i \frac{\partial \phi_i(\xi,\eta)}{\partial y} \tag{3.5}$$

where ξ and η are local coordinates within the element, and h_i and ϕ_i are the ice elevation and the shape functions, respectively, associated with the i^{th} node.

[1]This formulation assumes that the elements are quadrilateral and that the elements are approximately square and convex.

Thus to apply the gradient operator to a quantity defined at the nodes of an element, one needs only to substitute that quantity in for h_i in Equation 3.5.

The velocity U, however, is not defined at the nodes. Since U is calculated from ∇h, which involves all 4 nodes of an element, U has one value over the entire element. In order to find ∇U, we create a "pseudo-element" defined by the centers of the four elements that share a node. This is illustrated by the dotted line in Figure 3.1. One average value for the gradient of a velocity magnitude can then be found over this region by the same process as above:

$$\nabla U(\xi,\eta) = \hat{\mathbf{i}} \sum_{i=1}^{4} U_i \frac{\partial \phi_i(\xi,\eta)}{\partial x} + \hat{\mathbf{j}} \sum_{i=1}^{4} U_i \frac{\partial \phi_i(\xi,\eta)}{\partial y} \tag{3.6}$$

Here, U_i is the magnitude of the velocity at the i^{th} node of the "pseudo-element," which corresponds to the center of a real element.

Using a 3×3 block of elements, four "pseudo-elements" can be defined, each sharing the center (real) element as one node. Four values of ∇U — and hence $\frac{\partial U}{\partial l}$ — can be found, which correspond to nodes N1 through N4 in Figure 3.1. The same procedure can then be applied to these four values to find $\frac{\partial^2 U}{\partial l^2}$ for the element in the center of the 3×3 block. To obtain a value of $\frac{\partial U}{\partial l}$ for the center element, the four values from the "pseudo-elements" are averaged.

The velocities of the nine elements in the 3×3 block can have different directions. Thus, in the calculations for a given element (the center of the block), the components of the velocities in the direction of flow of that element are used. Call this component U_l. Then

$$U_l = \hat{m} \cdot \vec{U} = m_x U_x + m_y U_y \tag{3.7}$$

So we now have

$$\frac{\partial U_l}{\partial l} = \hat{m} \cdot \nabla(\hat{m} \cdot \vec{U}) \tag{3.8}$$

$$= m_x \sum_{i=1}^{4} (U_l)_i \frac{\partial \phi_i(\xi,\eta)}{\partial x} + m_y \sum_{i=1}^{4} (U_l)_i \frac{\partial \phi_i(\xi,\eta)}{\partial y} \tag{3.9}$$

and

$$\frac{\partial^2 U_l}{\partial l^2} = \hat{m} \cdot \nabla \left(\frac{\partial U_l}{\partial l} \right) \tag{3.10}$$

$$= m_x \sum_{i=1}^{4} \left(\frac{\partial U_l}{\partial l} \right)_i \frac{\partial \phi_i(\xi,\eta)}{\partial x} + m_y \sum_{i=1}^{4} \left(\frac{\partial U_l}{\partial l} \right)_i \frac{\partial \phi_i(\xi,\eta)}{\partial y} \tag{3.11}$$

These equations are implemented in the module **nconst.f** of the new program.

3.2 The Lookup Table ikx

In order to efficiently calculate the spatial derivatives as described above, there must be a way to locate quickly all the elements that share a given node. The lookup table **ikx** does this.

In both versions of the program, the data structure **KX** provides a way to look up the node numbers associated with a given element. The variable is dimensioned **KX**(**NUMEL**,4) (where **NUMEL** stands for the number of elements in the finite element grid), so that, for example, **KX**(124,2) gives the number of the second node of element 124. The **KX** data structure is illustrated in Table 3.1.

In order to calculate spatial derivatives using groups of elements, there must be a way of looking up this information in the other direction: a data structure is needed which yields the numbers of all the elements sharing a given node. This new data structure — an "inverted **KX**" — is called **ikx** in the new version of the program, and is illustrated in Table 3.2. Row number i contains the global numbers of the elements that share that node. If the input

Table 3.1: Example lookup table **KX**.

Global element number	Global node numbers
1	1 2 5 6
2	5 6 7 8
3	7 8 11 12
⋮	⋮

Table 3.2: Example lookup table **ikx**.

Global node number	Global element numbers	Count
1	1	1
2	7 8	2
3	9 6 11 12	4
⋮	⋮	⋮

node number is on a corner of the grid, then only only one element will contain that node, as node 1 in the example. If the input node is on the edge of the grid, two elements will share that node, as node 2 in the example. All internal nodes are shared by four elements. The structure **ikx** also contains an entry for the number of elements that share the given node; this is labeled "count" in Table 3.2.

To create **ikx**, the program loops through all the elements, inserting them into the table. After this, since the centers of elements sharing a node are used to construct a "pseudo-element," the elements listed in **ikx** are put in counterclockwise order.

3.3 Averaging

It is necessary to take a weighted, spatial average of the element velocities, before taking spatial derivatives of the velocity field, in order to average out numerical round-off errors and other sources of sharp transitions in velocity. It is also desirable to average over a "coupling length," which is related to the ice rheology and is generally measured in terms of ice thickness [17]. This averaging is done only in the calculation of the velocity gradients, and does not directly affect the actual velocity field as computed by the model.

The averaging scheme here can be elucidated by the following one-dimensional example, illustrated in Figure 3.2. Assume an evenly spaced series of six points (asterisks in Figure 3.2) which are values of a function of one variable x. Call this series (y_1, y_2, y_3, y_4, y_5, y_6). We can average each pair of adjacent points to get a new series of five points $\frac{y_1+y_2}{2}$, $\frac{y_2+y_3}{2}$, $\frac{y_3+y_4}{2}$, $\frac{y_4+y_5}{2}$, $\frac{y_5+y_6}{2}$. Call these points (y'_1, y'_2, y'_3, y'_4, y'_5). The locations of these points are midway between the original set of points, and are marked with diamonds in Figure 3.2.

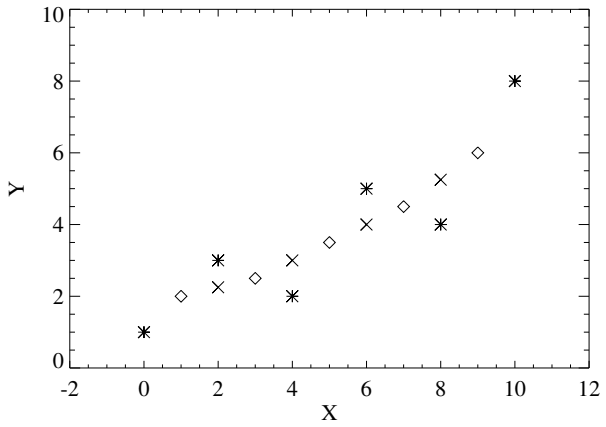

Figure 3.2: Example points in one dimension

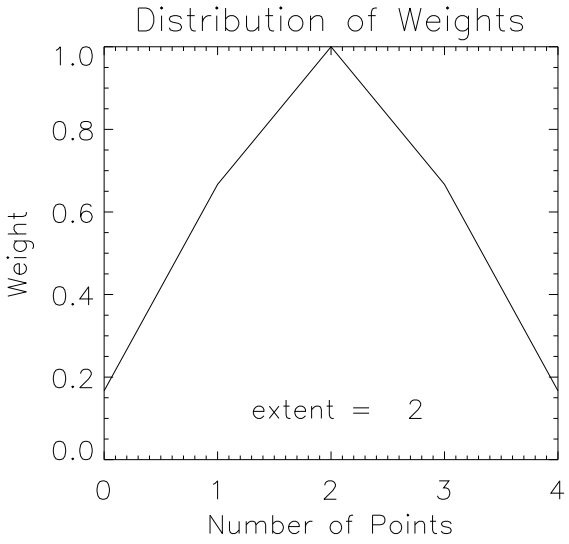

Figure 3.3: Weights in one dimension, with extent = 2.

We can do this process again to get a new set of points: ($\frac{y_1'+y_2'}{2}$, $\frac{y_2'+y_3'}{2}$, $\frac{y_3'+y_4'}{2}$, $\frac{y_4'+y_5'}{2}$), or (y_1'', y_2'', y_3'', y_4''). These are marked with '$\times$'s in Figure 3.2.

The point y_1'', which has the same x-coordinate as y_2, is a weighted average of the points y_1, y_2, and y_3:

$$y_1'' = \frac{1}{2}\left(\frac{y_1+y_2}{2}+\frac{y_2+y_3}{2}\right) \tag{3.12}$$

$$= \frac{1}{4}(y_1+2y_2+y_3) \tag{3.13}$$

Likewise, $y_2'' = \frac{1}{4}(y_2+2y_3+y_4)$, $y_3'' = \frac{1}{4}(y_3+2y_4+y_5)$, and $y_4'' = \frac{1}{4}(y_4+2y_5+y_6)$.

This process can be repeated — averaging the averages — effectively incorporating more points into the averages. Doing the averaging twice, as above, each point in the original list is averaged with one neighboring point on either side. If the process is repeated twice again, each point in the original series will be averaged with two neighboring points on either side. In this case,

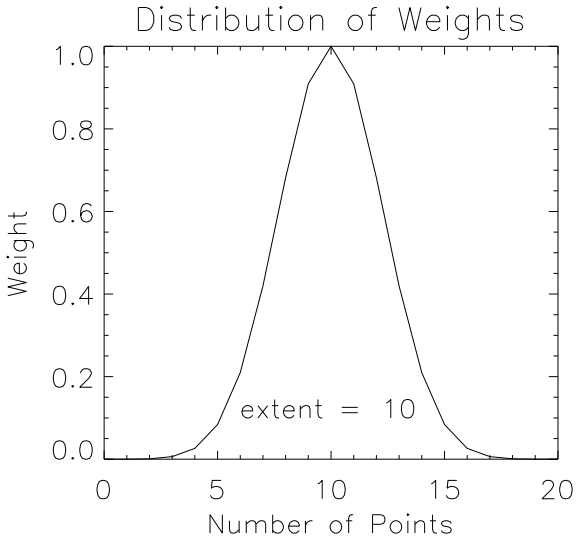

Figure 3.4: Weights in one dimension with extent = 10.

the average at the same location as y_3 would be

$$\begin{aligned} y_1''' &= \frac{1}{4}\left[\frac{1}{4}(y_1 + 2y_2 + y_3) + 2\frac{1}{4}(y_2 + 2y_3 + y_4) + \frac{1}{4}(y_3 + 2y_4 + y_5)\right] \\ &= \frac{1}{16}(y_1 + 4y_2 + 6y_3 + 4y_4 + y_5) \end{aligned} \tag{3.14}$$

Thus if the averaging procedure is done $2n$ times, then a given point will be averaged together with n neighbors on each side. The case above, where the weights are $\frac{1}{16}(1, 4, 6, 4, 1)$, is illustrated in Figure 3.3, and corresponds to the variable "extent" (in this one-dimensional case, the number of points on each side that are averaged into the center point) being equal to 2. In Figure 3.4, the weight distribution is shown when extent = 10. This averaging method yields weight distributions similar in shape to the weighting functions in [17], where Kamb and Echelmeyer show that the longitudinal coupling effects of a perturbation decay with distance from the perturbation as

$$e^{\frac{-|x'-x|}{l}} \tag{3.15}$$

where x' is the location of the perturbation, and l is the so-called "longitudinal coupling length." This function is illustrated in Figure 3.5; the perturbation is at $x = 50$.

In two dimensions, the starting set of points is on a regular rectangular grid, as illustrated in Figure 3.6. One averaging step produces the average of four points defining a unit square (denoted by closed circles in Figure 3.6), and the averaged point is located at the center of the square, as marked by the squares in Figure 3.6. One more step produces averages of these averages; these new values are associated with the original node sites (closed circles). Analogous to the one dimensional case, if the averaging process is carried out $2n$ times, then a given point will have n levels of surrounding points averaged

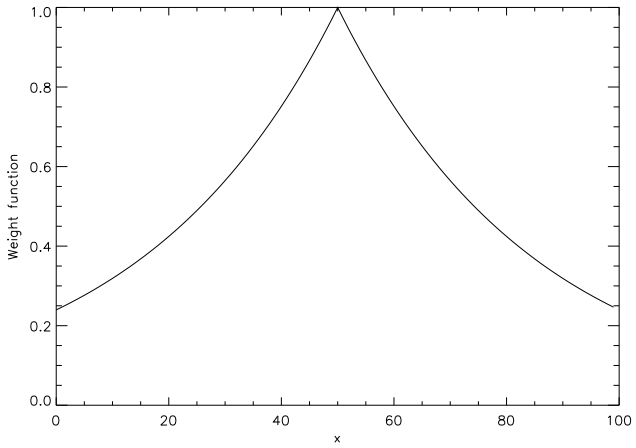

Figure 3.5: Form of weight function of Kamb and Echelmeyer.

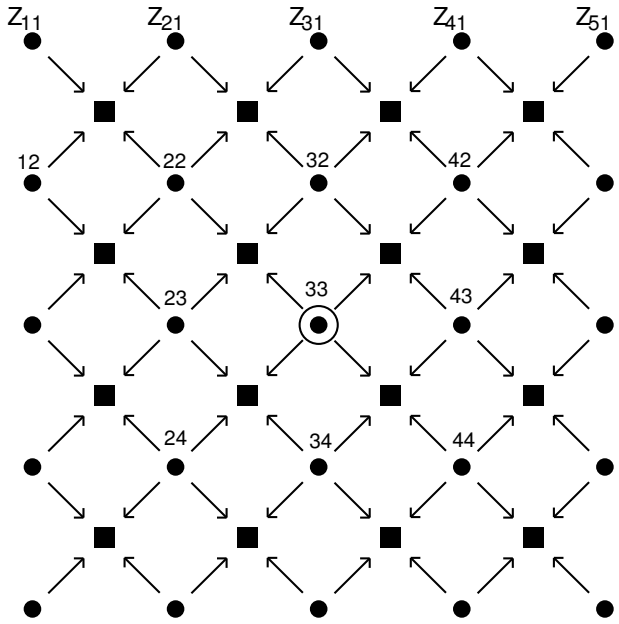

Figure 3.6: Example points in two dimensions

in with it. In Figure 3.6, all the points will be averaged into the center one (marked with an open circle) if four averaging steps are carried out (extent = 2). After one averaging step, the point immediately up and left from the center point (marked with a square) would have a value $z'_{11} = \frac{1}{4}(z_{22} + z_{32} + z_{23} + z_{33})$. After the second average (corresponding to extent = 1), the center point (at z_{33}) would have the value

$$\begin{aligned} z''_{11} &= \frac{1}{4}(z'_{11} + z'_{12} + z'_{21} + z'_{22}) \\ &= \frac{1}{4}\left[\frac{1}{4}(z_{22} + z_{32} + z_{23} + z_{33}) + \frac{1}{4}(z_{32} + z_{42} + z_{33} + z_{43})\right. \\ &\quad \left. + \frac{1}{4}(z_{23} + z_{33} + z_{24} + z_{34}) + \frac{1}{4}(z_{33} + z_{43} + z_{34} + z_{44})\right] \\ &= \frac{1}{16}(z_{22} + z_{42} + z_{24} + z_{44} + 2z_{32} + 2z_{23} \\ &\quad + 2z_{43} + 2z_{34} + 4z_{33}) \end{aligned} \tag{3.16}$$

Figure 3.7 shows the distribution of weights when extent = 2.

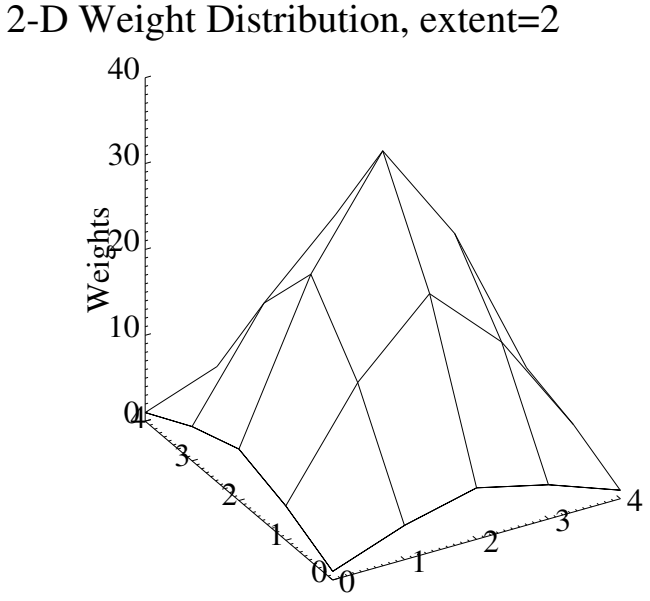

Figure 3.7: Weights in 2-D

CHAPTER 4

SIMULATION OF A SIMPLE SLAB: COMPARISON OF OLD AND NEW MODELS

This chapter describes a simple model of a block of ice, simulated using the finite element program both before and after the stress coupling modifications. This comparison is used to illustrate the effect of the new longitudinal stress coupling.

4.1 Geometry

In this experiment, the input model consisted of a rectangular, finite slab of ice placed on a surface which was horizontal in half the region, and inclined in the other half of the region. The slab was 'grown' using the finite element program by specifying a positive mass balance in a rectangular region in the center of the grid. No basal sliding was allowed during this stage. Figure 4.1 is a three-dimensional representation of the resulting input configuration. The slab is approximately 5200 m $\times$ 5200 m horizontally; the thickness is about 140 m in the center. Note the large vertical exaggeration in Figure 4.1. This was chosen so that Figure 4.5, which shows the ice block after deformation and shares the same vertical scale with Figure 4.1, would be scaled appropriately.

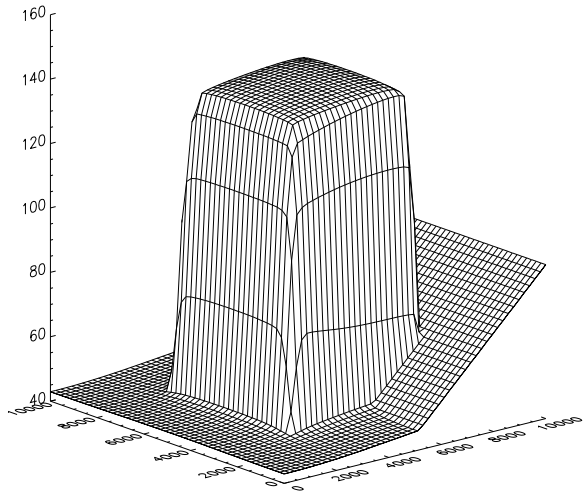

Figure 4.1: Finite Slab

4.2 Boundary Conditions

Once the slab had formed, a new set of boundary conditions was applied. A no-slip boundary condition was imposed in the inclined half-region; in the flat half of the grid, the ice moved by basal sliding only. (The variable f was set to 1 in the flat half of the grid, so that the velocity due to internal deformation became zero. See Chapter 2.) The sliding was considerably faster than the creep flow in this problem, so that the internal deformation of the sliding region was neglected. The boundary flux was specified to be zero around the perimeter of the grid. In both the creation of the initial geometry and the subsequent run, the ice was subjected only to body forces (gravity) and tractions at the bed.

4.3 Model Outputs

Figures 4.2 and 4.3 show longitudinal elevation profiles of the ice block as calculated by the model before and after the program modifications. The profiles in Figure 4.2 are from shortly after the start of the run, while those in Figure 4.3 are from near the end, when the ice had nearly flattened out.

In the old model, there is no coupling of forces between adjacent elements. Thus, the only way the faster speed of a steep section can propagate upstream is by gradually drawing down the ice thickness element by element, in turn giving these elements steeper slopes. Because this draw-down process takes many time steps, this model cannot capture more rapid dynamical processes, such as high extension rates propagating upstream.

By contrast, the longitudinal coupling implemented in the new model enables the effects of the steep section to be felt upstream and downstream — within the averaging distance ("extent") — in one time step.

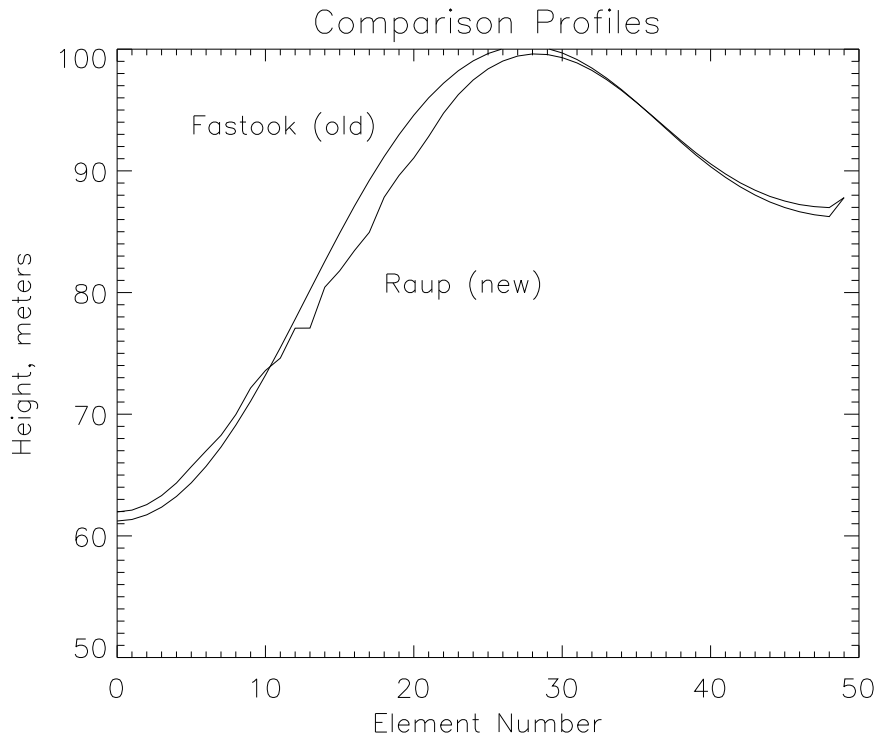

Figure 4.2: Elevation profiles from old and new models, close to start of run.

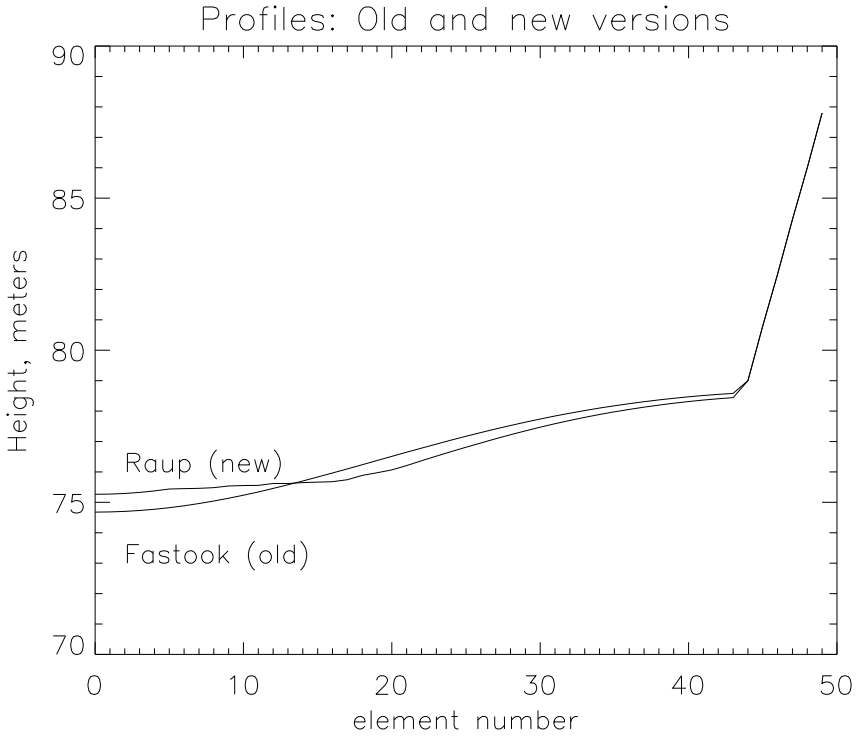

Figure 4.3: Profiles from old and new, near end of run.

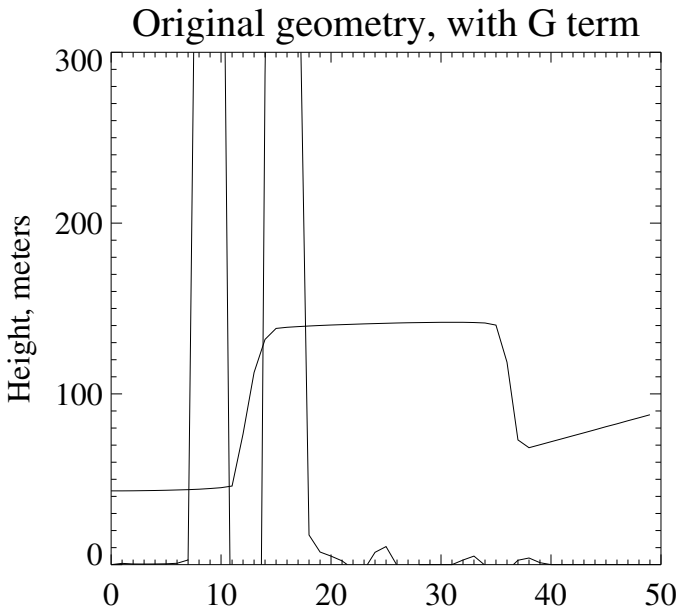

Figure 4.4: Sense of G

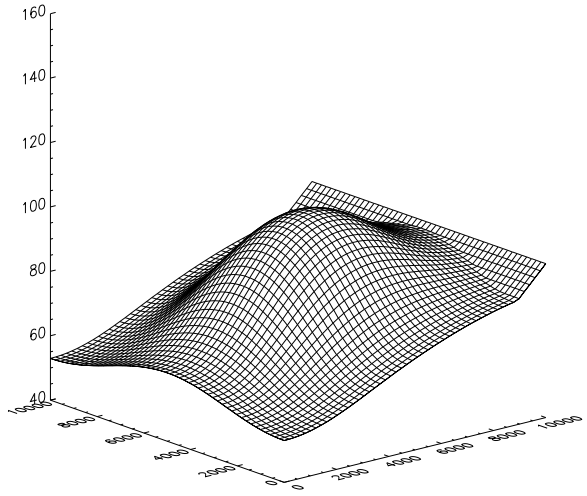

Figure 4.5: Finite slab, after start of run.

The velocity gradients from the previous time step are used to alter the driving stress in the current time step. Thus, as can be seen in the figures, a steep slope spreads and flattens out faster in the new model than in the old.

The new model shows faster spreading, and in this experiment, the G-term was typically of the same order of magnitude as the locally determined $\rho g h \sin\alpha$ term, though at the corners it was several orders of magnitude larger. This is an artifact of having an unrealistic geometry at the start of the run.

Figure 4.4 is a plot of G (nearly vertical lines), superimposed over a profile of the block. In the region between 7 and 11 on the horizontal axis, G is large and positive. Between 11 and 14, G is large and negative. Between 14 and 18 it is again positive. The result is that regions where G is positive move faster than they would without the coupling, and the region where G is negative moves slower. Restated, the steep section speeds up the flat sections on either side, and the flat sections slow down the steep section between them.

One may notice that the magnitude of G is considerably smaller at the steep section at the upstream (right) end. Since sliding was not allowed here, motion is due only to creep flow, and velocities and velocity gradients are therefore much lower. Notice also the region of positive G in the center of the block, where the basal boundary condition changes from no-slip to all sliding.

Figures 4.6 and 4.7 show the G-term for the two times over the entire domain of the problem. These figures show qualitatively the same properties of G as Figure 4.4: G is negative at the steep sections and positive at the flat parts on either side of the steep sections. Again, because of the no-slip boundary condition on the upstream half of the domain, the magnitude of G is low here.

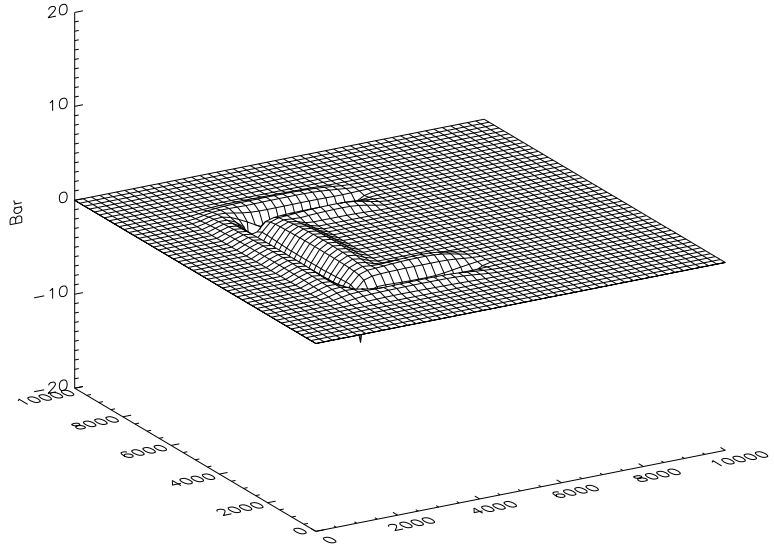

Figure 4.6: The G-term, shortly after beginning of run.

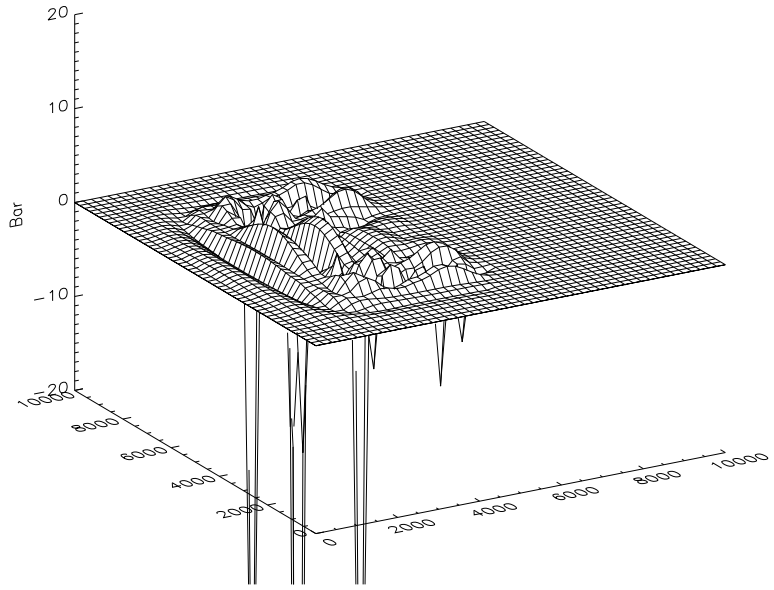

Figure 4.7: The G-term, near the end of run.

Because three numerical derivatives are being taken of the ice surface in the calculation of the G-term, sharp changes in geometry, as were part of the input model, tend to become amplified in the G-term in an oscillatory manor as time progresses. This effect can be dampened by selecting an appropriate value for the variable "extent," which determines the extent of spatial averaging done before derivatives are taken.

The amount of averaging done, and when it is done, has a large effect on the overall stability of the model. Decoupling the smoothing process from the averaging done in order to achieve the desired "coupling length" would be an improvement. It would allow, for example, smoothing to be done between the three derivatives, or just before the last one, to address the stability, while leaving the "coupling length" parameter independent. At the heart of this instability is the process of taking three consecutive numerical derivatives. The instability does not stem from the equations themselves. Thus, as long as the data can be appropriately smoothed before taking the derivatives, the model will produce meaningful results.

CHAPTER 5

SIMULATION OF THE ADVANCE OF ICE ACROSS HUDSON STRAIT

5.1 Introduction

The previous chapters discuss the theory behind improvements made to a finite element model for glacier flow. This chapter describes an application of this new model in the area of recent ice sheet reconstruction. In particular, the purpose of this simulation is to determine whether there are any glaciological constraints prohibiting a particular glacial advance which is indicated by land and marine records. The background of this event, dubbed the Gold Cove Advance, is described below.

Glacial cycles were once thought to follow a steady oscillating path between ice ages and interglacial periods in step with variations of energy input from the sun due to orbital irregularities. Climatological evidence (e.g. [13]) and atmospheric modeling efforts (e.g. [23]) have led the scientific community to conclude that both regional temperatures and ice sheet extent are much more variable than this, involving time scales on the order of 10^2–10^3 years rather than 10^4–10^5 as would be the case for purely orbital forcing [12].

The leading theory holds that ocean circulation is an important factor in influencing climate on time scales shorter than those of the solar forcing, at least in the Northern Hemisphere. The thermohaline circulation, the so-called "conveyor belt" proposed by Broecker and Denton [6], is driven by warm, relatively saline surface water flowing from the tropics to the North Atlantic,

where, due to cooling and evaporation, it becomes denser and sinks to form the North Atlantic Deep Water. It then flows south, east around Africa and India, and completes the cycle.

In the process, this conveyor pumps approximately 1 petaWatt (10^{15} Watts) of heat into the North Atlantic region [22], moderating the climate in this region. This keeps ice sheets relatively small, which keeps the albedo low in the northern hemisphere, enhancing the regional warming effects of insolation.

It is thought that the onset of glaciation could be triggered, at least in part, by the shutting down of this circulation [6, 7]. If the thermohaline circulation is disrupted, heat is no longer pumped in such large quantities into the northern hemisphere, and ice sheets can expand. An influx of low-density fresh water into the North Atlantic region could disrupt the thermohaline circulation by forming a buoyant lid which would prevent the warm tropic-originating water from becoming more dense by evaporation.

Temperature records based on isotopic analysis of ice cores, pollen records from the lands surrounding the northern Atlantic, and foraminifera records from the northern Atlantic itself, indicate that approximately 10,000 years ago,[1] when the world was warming and the northern ice sheets from the last ice age were retreating, there were sudden and short-lived periods of return to glacial conditions, exemplified by the Younger Dryas (e.g. [5]). Independently, isotopic and lithographic evidence from sea floor cores, as well as geomorphological evidence of outbursts from glacial lakes in North America indicate that large fluxes of both fresh glacial meltwater and icebergs flowed into the North Atlantic at several times, also approximately 10,000 years ago. It is theorized that these large fluxes of low-density fresh water were sufficient

[1] All dates given are uncalibrated ^{14}C dates.

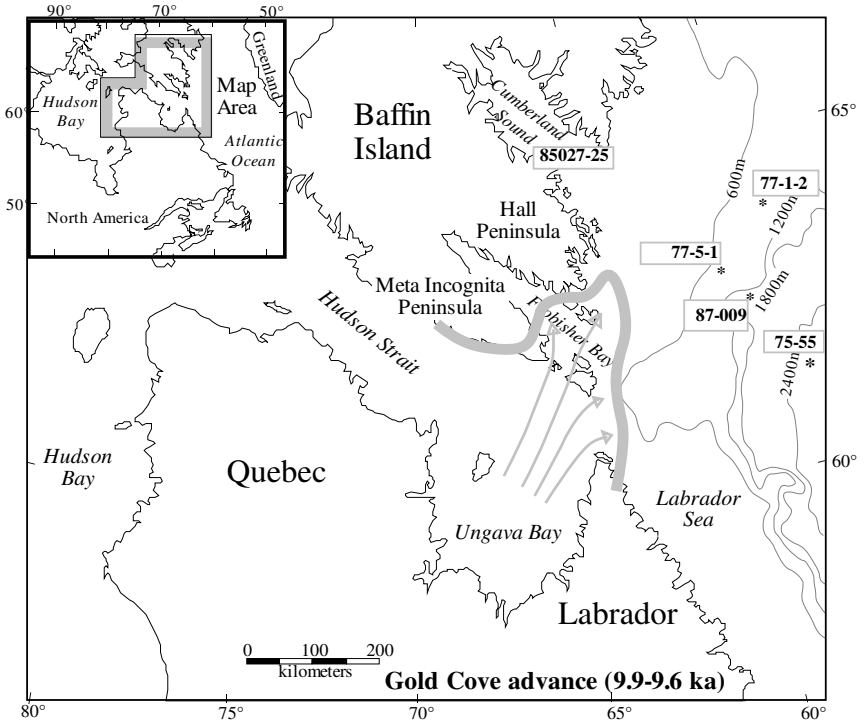

Figure 5.1. Detail of simulation area, also showing extent of ice during Gold Cove advance. (From [1] (base map) and [18] (ice extent))

to disrupt the sinking action of the saline waters in the North Atlantic, thereby shutting down or severely crippling the the conveyor circulation, and bringing on the Younger Dryas (11 ka to 10 ka before present [26]), and other more minor cooling events.

In [18], Kaufman *et al.* argue that at least two times following the Younger Dryas, ice has rapidly advanced across Hudson Strait from the Labrador region, producing in the process large quantities of icebergs. Geomorphological evidence on southern Baffin Island and the Labrador Peninsula indicates that ice moved in a north-northeastward direction from the Labrador Peninsula across Hudson Strait and onto Baffin Island [18, 19]. Two of these are labeled the Gold Cove advance (9.9–9.6 ka) and the Noble Inlet advance (8.9 ka). For the Gold Cove advance, bedrock striations on Meta Incognita and Hall Peninsulas clearly indicate not only the orientation of ice flow, but its sense as well. Additionally, morainal features and esker swarms surrounding Ungava Bay (see Figure 5.1) on Labrador Peninsula, as well as erratics with distinct provenance, indicate convergent northward flow into the Ungava Bay region [19].

The picture of ice advancing from Ungava Bay across Hudson Strait differs markedly from previous hypotheses of ice flowing toward the southeast along the axis of Hudson Strait. It may be that ice has indeed flowed along the axis of the Hudson Strait, but it is clear that this is not the only type of flow that has ever occurred.

Because Hudson Strait is relatively deep (400–900 m), objections have been raised to the possibility of a cross-strait flow pattern based on glaciological grounds. The purpose of this simulation is to show that advance of ice out from

Ungava Bay across Hudson Strait is physically possible — i.e. that there are no glaciological constraints prohibiting such a Gold Cove-like advance. Iceberg calving fluxes are also estimated.

5.2 Model Inputs

As described in Chapter 1, the area of simulation included most of the Labrador Peninsula, centered at 56° N, 68° W, and covered 22° in latitude and 24° in longitude. The bedrock data come from a modern digital terrain model. The maximum height of the ice sheet was constrained by a geophysical reconstruction based on isostatic rebound calculations done by Peltier [30].

5.2.1 Initial Geometry An initial ice dome was "grown" by specifying a large positive mass balance over much of the peninsula, while allowing no sliding at the base. It should be noted that this growth process was carried out in order to produce a realistic ice dome over the existing terrain. This was not meant to model the formation of the actual ice sheet. This process was continued until the dome had reached a maximum height of approximately 2200 m. Knowledge of the margin locations for the dome was constrained by work of Kleman [19], who used marginal and subglacial depositional features such as eskers to constrain the extent of the ice, and to conclude that the ice dome had a core which was frozen to the bed. Since the ice sheet underwent creep flow during the growth process, it assumed a realistic shape.

5.2.2 Ice Flow Parameters As described in Chapter 2, Glen's flow law was used for the creep flow of ice (see [29]), $U_f \propto (\tau_b/A)^n$, with parameters $n = 3$ and $A = 3.0\,\text{bar year}^{1/3}$. Basal sliding was modeled using a Weertman sliding law (see [34]), $U_f \propto (\tau_b/B)^m$, with $B = 0.02\,\text{bar}\,\left(\frac{\text{year}}{\text{m}}\right)^{1/2}$ and $m = 2$.

Figure 5.2: Approximate outline of sliding region. North is up.

5.2.3 Spatial and Temporal Control of Sliding Once the ice dome had been placed on the peninsula, sliding was allowed to occur in Ungava Bay, all of Hudson Strait, and out to the continental shelf, as shown in Figure 5.2. This does not mean that sliding occurred everywhere in this region of the model, only that the parameter governing the rate of sliding allowed higher rates here than elsewhere. The parameters for sliding were spatially constant in this region.

As mentioned in the introduction to this chapter, evidence indicates that the core of the ice dome on the Labrador Peninsula was frozen to the bed [19], so that no sliding occurred there. There is, however, evidence of sliding near Ungava Bay and on Meta Incognita and Hall Peninsulas, and sliding is expected to have been possible (due to high basal water pressures) in Ungava Bay, Hudson Strait, and in the Labrador Sea, because of expected high basal water pressures there and the presence of sediments. The simplest boundary separating the sliding regions from the frozen regions was chosen (see Figure 5.2), taking into account all known evidence. Once selected, this sliding region was left alone; the region and the sliding parameters remained spatially and temporally constant.

5.2.4 Calving Calving is handled simply in this model. When the ice in an element reaches flotation — that is, its thickness is smaller than or equal to the thickness of ice that could be buoyed by water of the depth at that element — then the ice "calves." In this case, "calving" means that the ice thickness for that element is set to zero. Calving flux for a given element that has calved is calculated by determining the product of velocity, ice thickness, and element width.

A more physically based relation — perhaps based on an empirical relation to strain-rate, or even on a rigorous treatment from the point of view of fracture mechanics — is desirable and is a goal of further research within the project of which this thesis work is a part. The simple flotation relation was chosen for its simplicity, as well as its seemingly good correspondence to actual calving rates in temperate ice.

5.2.5 Mass Balance One of the terms in the continuity equation solved by this model is the mass balance term (see Equation 2.1). This term can be explicitly specified, or, as in this experiment, can be calculated at each time step as a function of ice surface elevation, $\dot{a} = f(h(x, y))$, using a scheme developed by Fastook. The fitting function used is a piece-wise linear function, which assumes a constant accumulation rate for the high elevation, interior portion of the dome at high elevation, then fits three line segments between there and the maximum ablation rate at the margin. The two inflection points between are at the elevation of peak accumulation and the equilibrium elevation. This is illustrated in Figure 5.3.

In this scheme, six numbers must be specified:

AMARG	ablation rate at margin (negative number, ma^{-1})
APEAK	maximum accumulation rate (positive number, ma^{-1})
ADOME	uniform high-elevation accumulation rate (ma^{-1})
HE	equilibrium line elevation (m)
HP	elevation of peak accumulation (m)
HM	elevation at which ADOME begins (m)

For this experiment, AMARG $= -1.0\,\mathrm{ma}^{-1}$, APEAK $= 0.2\,\mathrm{ma}^{-1}$, ADOME $= 0.1\,\mathrm{ma}^{-1}$, HE $= 400\,\mathrm{m}$, HP $= 1500\,\mathrm{m}$, and HM $= 1900\,\mathrm{m}$.

Figure 5.3: Schematic diagram of mass balance model.

5.2.6 Averaging The variable "extent" controls the amount of averaging applied to the velocity field before spatial gradients are taken. This process is described in detail in Section 3.3. The value of "extent" was generally set to 2.

5.2.7 Model Time Three time parameters are input into this model. Values used in this experiment are given in parentheses.

(1) Number of time steps in run (50).

(2) Number of time steps to skip between data dumps (5).

(3) Number of years per time step (20).

5.3 Model Results

Figures 5.4 through 5.7 show an output sequence from the program. Vertical exaggeration is approximately 150:1; units of all axes are kilometers.

With rapid sliding enabled under the ice covering Ungava Bay (see the slump in the ice at the approximate coordinates (-1700, 3400) in Figures 5.4 through 5.7), this ice immediately began moving out in a north-northeastward direction toward Baffin Island, averaging speeds of approximately $500\,\mathrm{m\,a^{-1}}$. This is comparable to speeds of modern Antarctic ice streams, which typically flow at about $450\,\mathrm{m\,a^{-1}}$ [32]. Longitudinal strain-rates were typically $0.001\,\mathrm{a^{-1}}$ to $0.3\,\mathrm{a^{-1}}$, and occasionally were as high as $1\,\mathrm{a^{-1}}$.

The ice front crossed the 200 km of Hudson Strait and reached Meta Incognita Peninsula on Baffin Island in approximately 400 model years; at this point, the flow slowed. The modeled direction of ice flow on Meta Incognita and Hall Peninsulas (approximately 10 ± 4 degrees east of north) is consistent with the orientation of bedrock striations observed there [18].

The presence of an ice front in the relatively deep water of Hudson

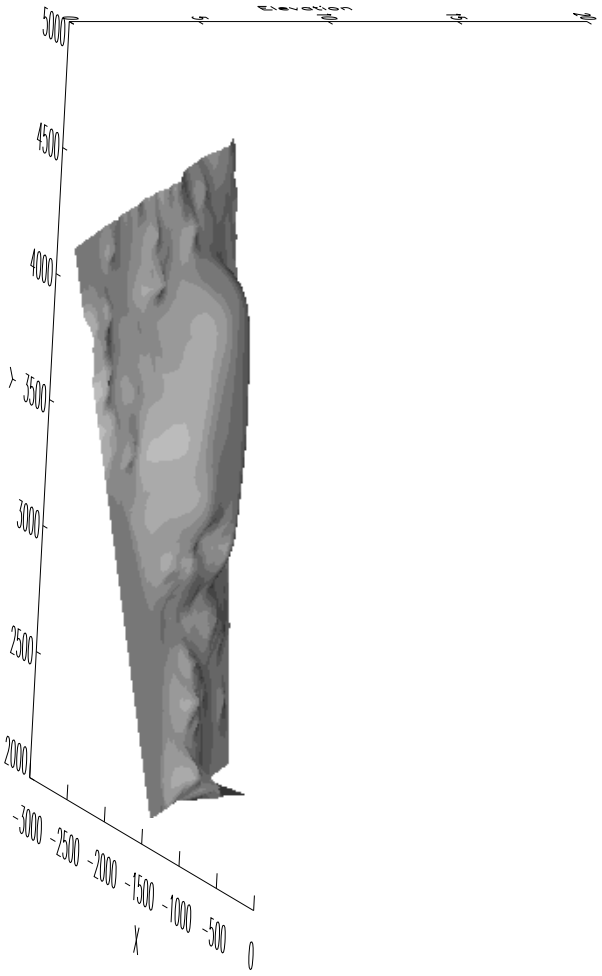

Figure 5.4: Ice dome at 100 model years.

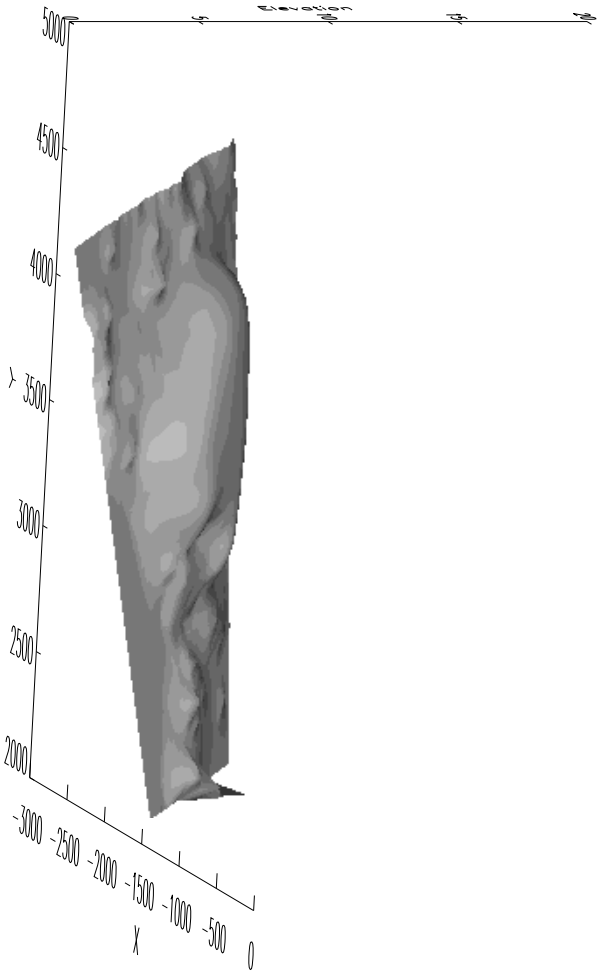

Figure 5.5: Ice dome at 300 model years.

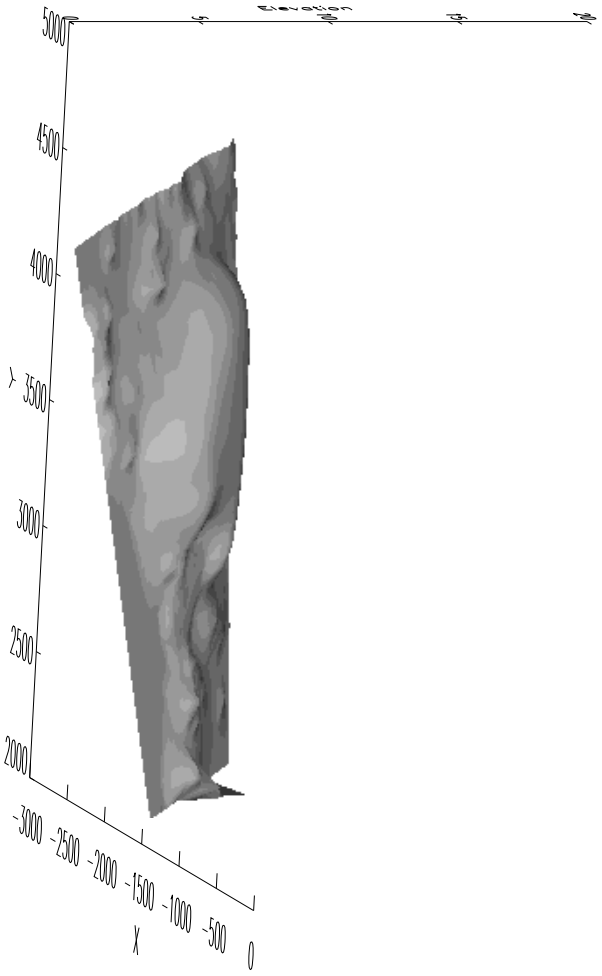

Figure 5.6: Ice dome at 600 model years.

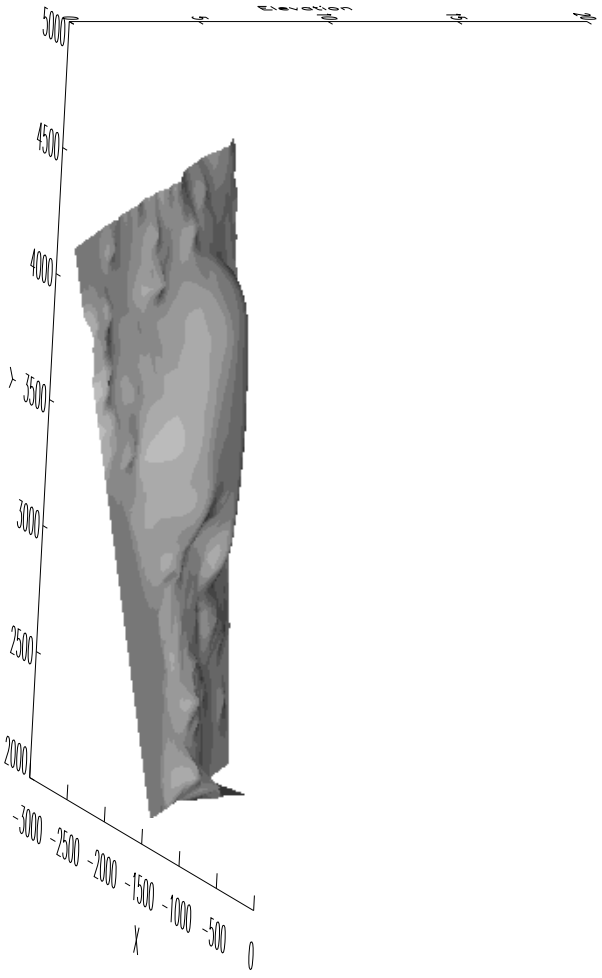

Figure 5.7: Ice dome at 1000 model years.

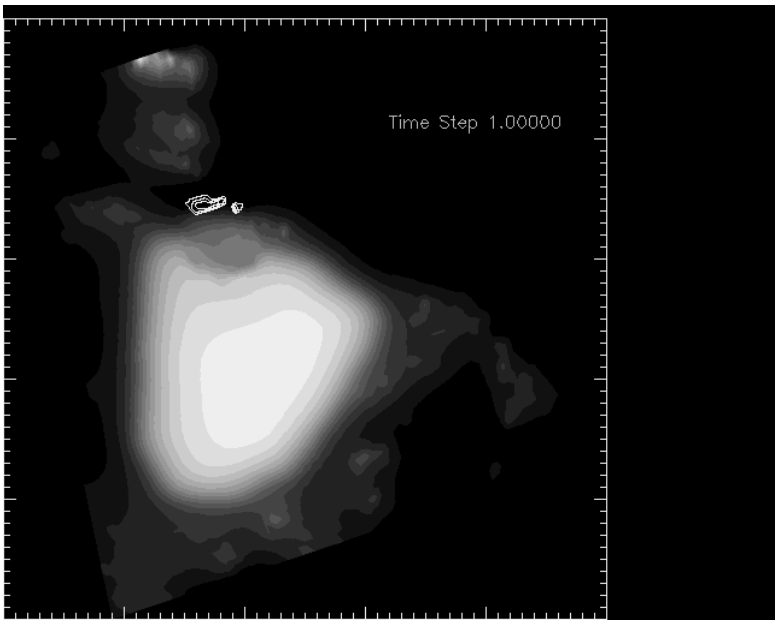

Figure 5.8: Calving at 100 model years.

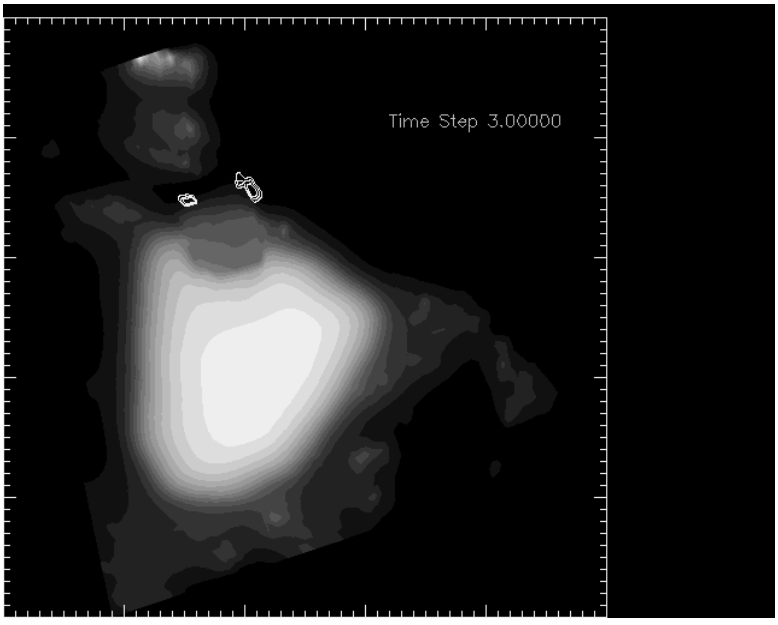

Figure 5.9: Calving at 300 model years.

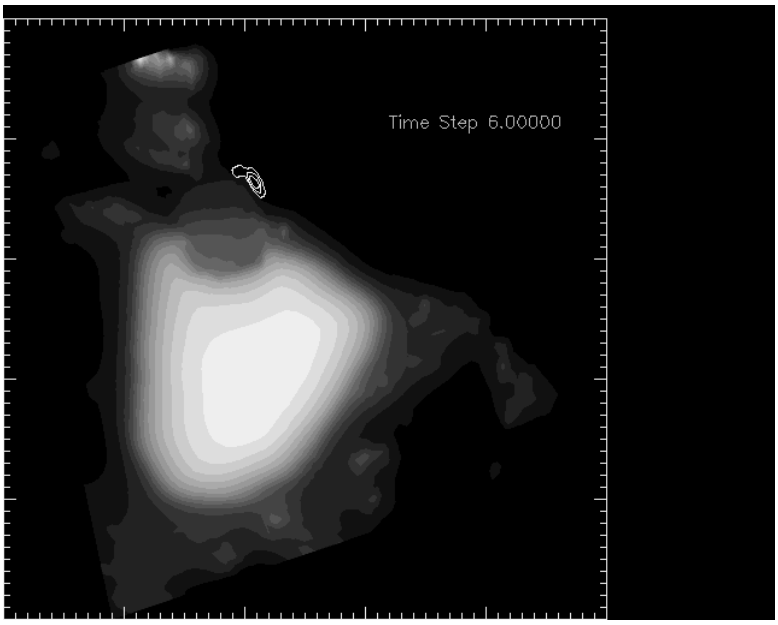

Figure 5.10: Calving at 600 model years.

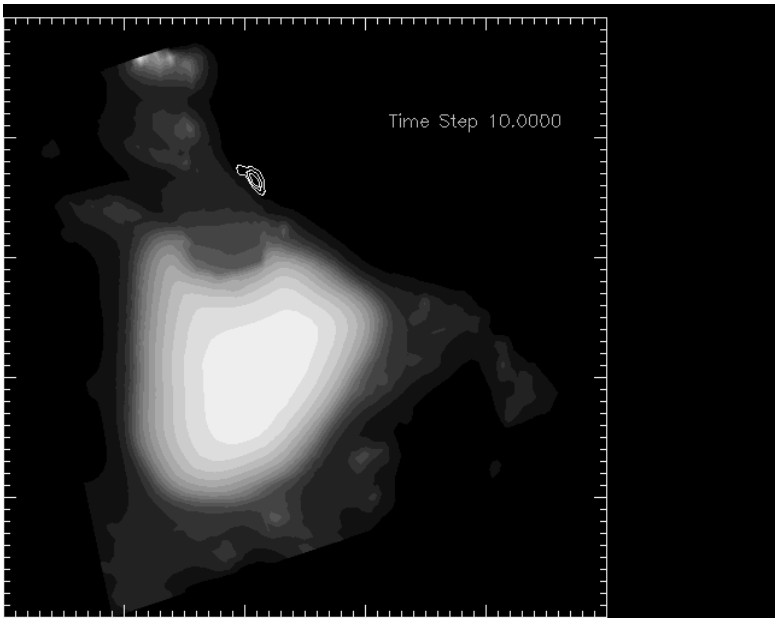

Figure 5.11: Calving at 1000 model years.

Strait (approximately 600 m) led to high calving rates and iceberg discharge. Figures 5.8 through 5.11 are map views (with north approximately upward) of the modeled region, with the ice dome represented by the shaded region in the lower portions of the figures, and southern Baffin Island toward the top. The small white contour lines mark regions of high calving rates. Figure 5.12 shows the total calving flux (in water equivalent) as a function of model time.

The region of highest calving followed the ice front across Hudson Strait. When the ice reached Meta Incognita Peninsula, the region of highest calving moved to the east side of the ice tongue, which was still exposed to relatively deep open water. Since the amount of ice exposed to open water was less at this point, total calving flux decreased. The significance of the magnitude of the calculated calving fluxes is discussed in Section 5.5.

5.4 Sensitivity of Results to Input Parameters

The final run in which the ice succeeded in crossing Hudson Strait and over-riding the Meta Incognita Peninsula was used as the control run. The values of the parameters in this run were given in the previous section.

The parameters investigated are as follows:

h_0	Initial height of ice dome.
τ_0	Value of longitudinal stress where G-term crosses from linear to non-linear.
B	Sliding constant.
A	Glen's flow constant.
E (extent)	Degree of averaging.

The number of time steps was also varied, with little change in results. The results of the parametric sensitivity study are summarized in Table 5.1.

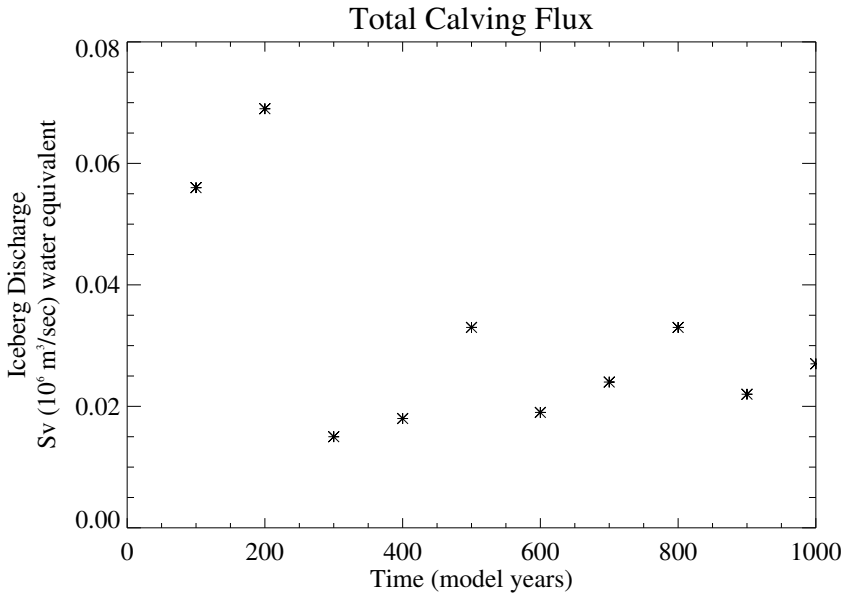

Figure 5.12: Calving flux versus model time.

The information in the table is abbreviated in order to make comparison of the relative effects of the different parameters easy.

The initial peak elevation of the ice dome h_0 was critical in determining whether ice crossed Hudson Strait. This model showed that the ice must have been more than 2000 m thick when the rapid motion began in order for the ice to make it to Baffin Island. This fits within the constraints of Peltier's reconstruction [30].

The parameter τ_0, explained in detail in Section 2.3, ideally should be as small as possible. The actual rheology of ice is non-linear; the denominator of the G-term is linearized in the region of small strain-rates here only to avoid singularity of the equations. That the model results are similar for both small values of τ_0 shows that the choice of the exact value of this parameter was not important, as long it was ≤ 0.5.

The sliding constant B was a determining factor in whether ice crossed the strait. While it is felt that the value used here was realistic and consistent with other modeling efforts, better understanding of sliding processes should be a future priority.

The model results showed moderate sensitivity to the value of the flow constant A. However, this parameter is fairly well constrained by experiment, and was varied in this sensitivity test beyond those experimental constraints [10, 29]. In general, the value of A is a function of temperature. The value used in the control run ($A = 3$) corresponds to a temperature of $-7°$ C. The range of values of A used in the parameter sensitivity study corresponds to a temperature range of 0 to $-20°$ C.

Table 5.1: Parameters in Sensitivity Runs.

Parameter	**Value**	**Result/Comments**
Control Run		$h_0 = 2200\,\mathrm{m}$, $\tau_0 = 0.5$, $B = 0.02$, $A = 3$, $E = 2$
Initial Height (h_0) (Units: m)	1800	Ice did not cross strait.
	2000	Ice crossed strait half-way.
τ_0 (Units: bar)	0.125	Ice crossed strait, then retreated some.
	0.25	Ice crossed the strait.
	2.0	Ice did not cross strait.
Sliding Constant B (Units: bar $(\mathrm{year/m})^{1/2}$)	0.005	Crossed strait in first time step, then rapidly calved back into Ungava Bay. Unrealistically fast.
	0.01	Crossed strait in about 200 years, then calved back starting at about 700 years.
	0.04	Did not cross strait at all. Sliding was very slow.
Flow Constant A (Units: bar $\mathrm{year}^{1/3}$)	1	Ice crossed approx. 40% of strait.
	2	Ice crossed approx. 80% of strait.
	4	Crossed strait similarly to control run.
	5	Crossed rapidly, in approx. 200 a.
Extent (E) (Unitless)	1	Ice crossed strait rapidly; a bit numerically unstable. Massive retreat of ice front into dome.
	3	Ice crossed approx. 95% of strait.
	4	Ice crossed approx. 40% of strait.
	5	Ice crossed approx. 20% of strait.

5.5 Summary and Discussion

A principal result of this simulation is that the ice was modeled to cross from the Labrador Peninsula to Baffin Island. This happened in about 400 model years. The calving criterion used here — that of simple flotation — leads to the most rapid calving of any criterion. This is a strong requirement for calving; if ice can cross Hudson Strait under these conditions, it will also be able to cross under more realistic conditions which allow calving under more restricted conditions. This model thus indicates that under realistic glaciological conditions, an actual event of the nature of the proposed Gold Cove advance may have indeed occurred. That is, there are no glaciological grounds for excluding this type of cross-strait advance from consideration when reconstructing events around the time of the last deglaciation.

Secondly, the parameter sensitivity study indicates that the results depend on the initial height (elevation) of the ice dome. Given the parameters of this model, the ice dome must have been more than 2000 m thick, since the ice did not cross Hudson Strait with an ice dome initially 1800 m thick, and only half-crossed the strait with an initial thickness of 2000 m (see Table 5.1). This is consistent with the Peltier reconstruction, which puts the peak elevation of the Laurentian (North American) ice at approximately 2000 m above sea level [30].

The iceberg flux from an ice-surging event such as the one simulated here may have been sufficient to alter thermohaline ocean circulation. The calculated fluxes were on the order of 0.03 Sverdrups (1 Sverdrup $= 10^6$ m^{3}s^{-1}) water equivalent. The fresh water flux from the Atlantic to the Pacific via the atmosphere is 0.35 Sverdrups [5]; a fresh water input into the North Atlantic

on the order of one tenth of this is thought to be sufficient to disrupt or cripple the circulation [4]. For non-temperate ice (which evidence [19] indicates this was), calving rates may have been slower than was predicted from the simple "flotation calving" model used in this model; however, this flux prediction is a good first approximation. Other theories vie with the conveyor-belt model for acceptance as the explanation of irregularities in the paleoclimate record. This simulation indicates how one mechanism could affect ocean circulation, which in turn could affect global climate.

CHAPTER 6

CONCLUSIONS AND FUTURE WORK

6.1 Summary

The finite element model described in previous chapters, originally created by James Fastook for the purpose of modeling the formation and dynamics of ice sheets, was modified to include coupling of inter-element stresses along flow lines. This extension allowed the model to be more responsive to gradients in velocity or surface slope along flow lines. Previously, elements upstream from a region of higher velocity would respond to the faster flow only when the local gradient was made steeper by the ice thinning in the faster region. With the present modifications, the upstream ice will respond before this occurs.

This higher responsiveness improves the model's capability to simulate rapidly streaming flow. This model finds its best applications in situations where there is little divergence (positive or negative) in the flow, and where shear stresses due to transverse velocity gradients (e.g. $\partial u/\partial y$, where u is the x-component of velocity) have a small effect on the velocity distribution compared to the gravitational driving stress. In other words, these changes improve the model's capability to simulate normal stresses, but not shear stresses.

6.2 Future Work

Improvements can be made to the model in the areas of calving, stability, lateral stress coupling, the sliding law, and determining the value

for the averaging parameter "extent." Each of these is addressed below.

Part of the significance of the results of the previous chapter stems from the calculated iceberg fluxes, which of course depends on the particulars of the calving criteria used. In this model, as described before, ice calves only when and as soon as it reaches water deep enough to cause it to float. This criterion is a crude approximation of what may happen with temperate ice, but it is clearly inadequate for deeper investigations into fresh water fluxes and mechanisms related to the ocean conveyor circulation, particularly when cold ice is involved. Criteria based on fracture mechanics and/or strain rates are possible improvements.

In calculating the G-term that is added to the basal shear stress as a correction term, three numerical derivatives are taken of the ice elevation field. Because this is an inherently unstable process, smoothing is first applied. The smoothing, controlled in the program by the variable "extent," is currently done once before any derivatives are taken, but the application of smoothing just before the last derivative would decrease the numerical instability of this process.

The coupling of normal stresses in the model operates only along flow lines. There is no coupling of stresses perpendicular to the direction of flow. For example, given a flat inclined glacier in a valley, the velocity along the center of the glacier would be calculated to be too fast, since the shear stresses from the sides which act to slow a real glacier would not be felt. A scheme similar to the one implemented here for longitudinal coupling could possibly be used to incorporate coupling of lateral stresses as well.

The sliding law in this model is a simple empirical one which does not

incorporate effects from basal water pressure. Since the results of the previous chapter depend strongly on the sliding parameter B, this is an important area for improvement. In this work, a relation was tried which included the basal water pressure; however, the parameters in this relation proved difficult to tune, and the model results were quite unrealistic.

Finally, the value of the variable "extent," which controls the amount of averaging applied to the velocity field before derivatives are taken, should be dependent on the thickness of the ice, and should be separated from the parameter controlling smoothing (described above).

BIBLIOGRAPHY

[1] J. T. Andrews, H. Erlenkeuser, K. Tedesco, A. E. Aksu, and A. J. T. Jull. Late Quaternary (stage 2 and 3) meltwater and Heinrich events, Northwest Labrador Sea. **Quaternary Research**, 41:26–34, 1994.

[2] J. T. Andrews and K. Tedesco. Detrital carbonate-rich sediments, northwestern Labrador Sea: Implications for ice-sheet dynamics and iceberg rafting (Heinrich) events in the North Atlantic. **Geology**, 20:1087–1090, 1992.

[3] Eric B. Becker, Graham F. Carey, and J. Tinsley Oden. **Finite Elements: An Introduction**, volume 1. Prentice-Hall Inc., Englewood Cliffs, New Jersey, 1981.

[4] Wallace S. Broecker. Massive iceberg discharges as triggers for global climate change. **Nature**, 372:421–424, 1994.

[5] Wallace S. Broecker, Gerard Bond, and Millie Klas. A salt oscillator in the glacial Atlantic? 1. the concept. **Paleoceanography**, 5(4):469–477, 1990.

[6] Wallace S. Broecker and George H. Denton. The role of ocean-atmosphere reorganizations in glacial cycles. **Geochimica et Cosmochima Acta**, 53(10):2465–2501, 1989.

[7] Wallace S. Broecker and George H. Denton. What drives glacial cycles? **Scientific American**, pages 49–56, January 1990.

[8] W. F. Budd. The longitudinal stress and strain-rate gradients in ice masses. **Journal of Glaciology**, 9(55):19–27, 1970.

[9] W. F. Budd and N. A. Blundy. Empirical studies of ice sliding. **Journal of Glaciology**, 23(89):157–170, 1970.

[10] W. F. Budd and T. H. Jacka. A review of ice rheology for ice sheet modelling. **Cold Regions Science and Technology**, 16:107–144, 1989.

[11] W. F. Budd, D. Jenssen, and I. N. Smith. Three-dimensional time-dependent model of the West Antarctic Ice Sheet. **Annals of Glaciology**, 5:29–36, 1984.

[12] Peter U. Clark, Douglas R. MacAyeal, John T. Andrews, and Patrick J. Bartlein. Ice sheets play important role in climate change. **EOS**, 76(27), 1995.

[13] W. Dansgaard, S. J. Johnsen, H. B. Clausen, D. Dahl-Jensen, N. S. Gundestrup, C. U. Hammer, C. S. Hvidberg, J. P. Steffensen, A. E. Sveinbjörnsdottir, J. Jouzel, and G. Bond. Evidence for general instability of past climate from a 250 kyr ice-core record. **Nature**, 364:218–220, 1993.

[14] James L. Fastook. A map-plane finite-element model: Three modeling experiments. **Journal of Glaciology**, 35(119):48–52, 1989.

[15] James L. Fastook. A map-plane finite-element program for ice sheet reconstruction: A steady-state calibration with Antarctica and a reconstruction of the Laurentide Ice Sheet for 18,000 b.p. In H. U. Brown, editor, **Computer Assisted Analysis and Modeling on the IBM 3090**. IBM Scientific and Technical Computing Department, White Plains, NY, 1990.

[16] Barclay Kamb. Stress-gradient coupling in glacier flow: III. Exact longitudinal equilibrium equation. **Journal of Glaciology**, 32(112):335–341, 1986.

[17] Barclay Kamb and Keith A. Echelmeyer. Stress-gradient coupling in glacier flow: I. Longitudinal averaging of the influence of ice thickness and surface slope. **Journal of Glaciology**, 32(111):267–284, 1986.

[18] Darrell S. Kaufman, Gifford H. Miller, Jay A. Stravers, and John T. Andrews. Abrupt early Holocene (9.9–9.6 ka) ice-stream advance at the mouth of Hudson Strait, Arctic Canada. **Geology**, 21:1063–1066, 1993.

[19] Johan Kleman, Ingmar Borgström, and Clas Hättestrand. Evidence for a relict glacial landscape in Quebec-Labrador. **Palaeogeography, Palaeoclimatology, Palaeoecology**, 111:217–228, 1994.

[20] Bernd Kromer and Bernd Becker. German oak and pine ^{14}C calibration, 7200-9439 bc. **Radiocarbon**, 35:125–135, 1993.

[21] Scott J. Lehman. Ice sheets, wayward winds and sea change. **Nature**, 365:108–110, 1993.

[22] Scott J. Lehman, Daniel G. Wright, and Thomas F. Stocker. Transport of freshwater into the deep ocean by the conveyor. In W. R. Peltier, editor, **Ice in the Climate System**, volume 12 of **Global Environmental Change**, pages 187–209. NATO ASI Series I, 1993.

[23] S. Manabe and A. J. Broccoli. The influence of continental ice sheets on the climate of an ice age. **Journal of Geophysical Research**, 90:2167, 1985.

[24] George E. Mase. **Continuum Mechanics**. Schaum's Outline Series, McGraw-Hill, Inc., New York, 1970.

[25] Greenland Ice-Core Project (GRIP) Members. Climate instability during the last interglacial period recorded in the GRIP ice core. **Nature**, 364:203–207, 1993.

[26] Gifford H. Miller and Darrell S. Kaufman. Rapid fluctuations of the Laurentide ice-sheet at the mouth of Hudson Strait: New evidence for ocean/ice-sheet interactions as a control on the Younger Dryas. **Paleoceanography**, 5(6):907–919, 1990.

[27] John F. Nye. The effect of longitudinal stress on the shear stress at the base of an ice sheet. **Journal of Glaciology**, 8(53):207–213, 1969.

[28] W. S. B. Paterson. **The Physics of Glaciers**. Pergamon Press, 2nd edition, 1981.

[29] W. S. B. Paterson. **The Physics of Glaciers**. Pergamon Press, 3rd edition, 1994.

[30] W. Richard Peltier. Ice age paleotopography. **Science**, 265:195–201, July 1994.

[31] J. N. Reddy. **An Introduction to the Finite Element Method**. McGraw-Hill, Inc., 2nd edition, 1993.

[32] Theodore A. Scambos, Melanie J. Dutkiewicz, Jeremy C. Wilson, and Robert A. Bindschadler. Application of image cross-correlation to the measurement of glacier velocity using satellite image data. **Remote Sensing of the Environment**, 42:177–186, 1992.

[33] Minze Stuiver and Thomas F. Braziunas. Modeling atmospheric ^{14}C influences and ^{14}C ages of marine samples. **Radiocarbon**, 35(1):137–189, 1993.

[34] J. Weertman. The theory of glacier sliding. **Journal of Glaciology**, 5(39):287–303, 1964.

APPENDIX A

DERIVATION OF G

The following is a derivation of the so-called 'G term.' It is a correction to the expression for the basal shear stress in the plane strain model.

The following derivation assumes an infinitely wide glacier flowing down an inclined plane. The x-axis is defined to be along the flow direction, the z-axis is perpendicular to this and positive upwards; the y-axis points in the direction transverse to the direction of flow. The origin is at the bed, so that $z = 0$ there. The thickness of the ice is H, which is constant, and the angle of inclination of the slab is α.

We begin with the force equilibrium equations

$$\frac{\partial \sigma_{ij}}{\partial x_i} + f_j = 0$$

where σ_{ij} is the stress tensor, and f_j are body forces. In the x- and z-directions, this expands to

$$\frac{\partial \sigma_{xx}}{\partial x} + \frac{\partial \sigma_{yx}}{\partial y} + \frac{\partial \sigma_{zx}}{\partial z} + f_x = 0 \qquad \text{(A.1)}$$

$$\frac{\partial \sigma_{xz}}{\partial x} + \frac{\partial \sigma_{yz}}{\partial y} + \frac{\partial \sigma_{zz}}{\partial z} + f_z = 0 \qquad \text{(A.2)}$$

Because an infinitely wide glacier is assumed, deformation occurs in plane strain. Under this assumption, there is no variation in the y-direction, so $\frac{\partial}{\partial y} = 0$ Additionally, $f_x = \rho g \sin\alpha$ and $f_z = -\rho g \cos\alpha$. The previous equations thus reduce to

$$\frac{\partial \sigma_{xx}}{\partial x} + \frac{\partial \sigma_{zx}}{\partial z} + \rho g \sin\alpha = 0 \qquad \text{(A.3)}$$

$$\frac{\partial \sigma_{xz}}{\partial x} + \frac{\partial \sigma_{zz}}{\partial z} + -\rho g \cos\alpha \;\; = \;\; 0 \tag{A.4}$$

Rearranging Equation A.3 and integrating with respect to z from the bed to the surface, we have

$$\begin{aligned}
\sigma_{zx}|_H - \sigma_{zx}|_0 &= -\rho g \sin\alpha \int_0^H dz - \int_0^H \frac{\partial \sigma_{xx}}{\partial x} dz \\
-\sigma_{zx}|_0 &= -\rho g H \sin\alpha - H\overline{\frac{\partial \sigma_{xx}}{\partial x}} \\
\tau_b &= \rho g H \sin\alpha + H\left(\overline{\frac{\partial \tau_{xx}}{\partial x}} + \frac{\partial P}{\partial x}\right) \qquad \text{(A.5)} \\
&= \rho g H \sin\alpha + H\frac{\partial \bar{\tau}_{xx}}{\partial x} + H\frac{\partial \bar{P}}{\partial x} \qquad \text{(A.6)}
\end{aligned}$$

In the above, the overline signifies averaging in the vertical direction, and τ_b is the shear stress at the bed, $\sigma_{zx}|_0$. The only shear stresses at the surface are the ones due to wind currents. These are small compared to the forces within the glacier, so the surface shear stress ($\sigma_{zx}|_H$) is assumed to be zero. In getting to Equation A.5, the total stress σ_{xx} was replaced by the sum of the deviatoric stress τ_{xx} and the hydrostatic pressure P.

Next, Equation A.4 is rewritten, substituting the deviatoric stress and hydrostatic pressure for σ_{zz},

$$\frac{\partial \sigma_{xz}}{\partial x} + \frac{\partial \tau_{zz}}{\partial z} + \frac{\partial P}{\partial z} = \rho g \cos\alpha \tag{A.7}$$

To motivate the following steps, we want to derive an expression which includes a term $\partial \bar{P}/\partial x$. This is done by first differentiating the last equation with respect to x

$$\frac{\partial^2 \sigma_{xz}}{\partial x^2} + \frac{\partial^2 \tau_{zz}}{\partial x \partial z} + \frac{\partial^2 P}{\partial x \partial z} = 0 \tag{A.8}$$

then by integrating twice with respect to z, first from the surface down to an arbitrary depth, and secondly over the thickness:

$$0 \;\; = \;\; \int_0^H \int_H^z \frac{\partial^2 \sigma_{xz}}{\partial x^2} dz' dz + \int_0^H \int_H^z \frac{\partial^2 \tau_{zz}}{\partial x \partial z'} dz' dz + \int_0^H \int_H^z \frac{\partial^2 P}{\partial x \partial z'} dz' dz$$

$$0 = \int_0^H \int_H^z \frac{\partial^2 \sigma_{xz}}{\partial x^2} dz' dz + \int_0^H \left(\frac{\partial \tau_{zz}}{\partial x}\bigg|_z - \frac{\partial \tau_{zz}}{\partial x}\bigg|_H \right) dz + \int_0^H \left(\frac{\partial P}{\partial x}\bigg|_z - \frac{\partial P}{\partial x}\bigg|_H \right) dz \tag{A.9}$$

or, finally

$$\int_0^H \int_H^z \frac{\partial^2 \sigma_{xz}}{\partial x^2} dz' dz + H \frac{\partial \bar{\tau}_{zz}}{\partial x} + H \frac{\partial \bar{P}}{\partial x} = 0 \tag{A.10}$$

Again, the overlines signify averaging in the z-direction. Everywhere at the surface, both P and τ_{zz} are zero (atmospheric pressure is negligible compared to pressures in the ice), thus, in the above equation, the two terms evaluated at H ($\partial \tau_{zz}/\partial x|_H$ and $\partial P/\partial x|_H$) are equal to zero. This is because, with the constant-slope assumption, as the position of a point at the surface varies in the x-direction, it stays at the surface.

Combining with Equation A.6, we have

$$\int_0^H \int_H^z \frac{\partial^2 \sigma_{xz}}{\partial x^2} dz' dz + H \frac{\partial \bar{\tau}_{zz}}{\partial x} - \rho g H \sin\alpha - H \frac{\partial \bar{\tau}_{xx}}{\partial x} + \tau_b = 0 \tag{A.11}$$

The continuity equation for an incompressible medium (as ice is assumed to be) is

$$\nabla \cdot \vec{v} = 0, \quad \text{or} \quad \frac{\partial u}{\partial x} + \frac{\partial v}{\partial y} + \frac{\partial w}{\partial z} = 0 \tag{A.12}$$

In plane strain, this becomes

$$\frac{\partial u}{\partial x} = -\frac{\partial w}{\partial z} \tag{A.13}$$

Assuming τ_{xx} and τ_{zz} are related to the velocity components as

$$\tau_{xx} = 2\eta \frac{\partial u}{\partial x} \quad \text{and} \quad \tau_{zz} = 2\eta \frac{\partial w}{\partial z} \tag{A.14}$$

where η is a viscosity parameter, then it follows from equation (6) that

$$\tau_{xx} = -\tau_{zz} \tag{A.15}$$

Substituting Equation A.15 into Equation A.11, we obtain

$$\begin{aligned} \tau_b &= \rho g H \sin\alpha + 2H\frac{\partial \bar{\tau}_{xx}}{\partial x} - \int_0^H \int_H^z \frac{\partial^2 \sigma_{xz}}{\partial x^2} dz' dz \\ &= \rho g H \sin\alpha + 2G - T \end{aligned} \tag{A.16}$$

The letters G and T in Equation A.16 are common notation in the glaciological literature. In this paper, the T term is neglected.

For small values of the surface slope angle α, $\sin\alpha \approx \alpha \approx \tan\alpha = |\nabla h|$ when α is measured in the direction of the maximum slope. In Fastook's model, $|\nabla h|$ is used; this paper adopts this also, so that

$$\tau_b = \rho g H |\nabla h| + 2G \tag{A.17}$$